Highlights

Dynamic and modal analysis of nearly incompressible structures with stabilised displacement-volumetric strain formulations

Rubén Zorrilla, Riccardo Rossi, Ramon Codina

- Dynamic and modal analysis of linear elastic incompressible solids
- Stabilised mixed displacement and volumetric strain formulation
- Convenient linear and symmetric generalised eigenvalue problem

Dynamic and modal analysis of nearly incompressible structures with stabilised displacement-volumetric strain formulations

Rubén Zorrilla[a,b], Riccardo Rossi[a,b,*], Ramon Codina[a,b]

[a]*Departament d'Enginyeria Civil i Ambiental, Universitat Politècnica de Catalunya (UPC), Barcelona, 08034, Spain*
[b]*International Center for Numerical Methods in Engineering (CIMNE), Barcelona, 08034, Spain*

Abstract

This paper presents a dynamic formulation for the simulation of nearly incompressible structures using a mixed formulation and equal-order finite element interpolation pairs. Specifically, the nodal unknowns are the displacement and the volumetric strain component, something that makes possible the reconstruction of the complete stain at the integration point level and thus enables the use of strain-driven constitutive laws. Furthermore, we also discuss the resulting eigenvalue problem and how it can be applied for the modal analysis of linear elastic solids. The article puts special emphasis on the stabilisation technique used, which becomes crucial in the resolution of the generalised eigenvalue problem. In particular, we prove that using a variational multiscale method assuming the sub-grid scales to lie in the finite element space orthogonal to that of the approximation, namely the Orthogonal Sub-Grid Scales (OSGS), results in a convenient linear and symmetric generalised eigenvalue problem. The correctness, convergence and performance of the method is proven by solving a series of two- and three-dimensional examples.

Keywords: Modal analysis, Incompressible elasticity, Eigenvalue problems, Stabilised finite element methods, Variational multiscales, Orthogonal sub-grid scales

1. Introduction

The numerical simulation of deformable bodies involving incompressibility is a problem of interest in many engineering applications. Some examples are the performance analysis of rubber devices such as the elastomeric bearing pads present in bridge supports or the ultimate load analysis of metal component undergoing plasticity. It is a known issue that standard displacement-based (i.e., irreducible) formulations suffer from the so called volumetric locking phenomenon when undergoing deformations under incompressibility constraints, something that turns into an artificial stiffening that yields a wrong estimation of the mechanical response. Such limitation has been historically treated by targeting the calculation of a more accurate strain field capable to account for such kind of deformation. On the one hand, there are methods that achieve this by using the neighbours to compute an enriched displacement or strain field [1, 2]. On the other hand, one can modify the formulation by complementing the displacement unknowns with other variable(s), from which the enriched strain can be obtained. Such variable(s) addition, which leads to a mixed formulation problem, is the approach we focus on in this work.

It can be easily guessed that the nature of the resulting mixed formulation mainly depends on the extra variable(s). Specifically, the finite element interpolation of the mixed problem may result in an unstable formulation if it does not accomplish with the inf–sup condition. A very popular example of an (almost) inf-sup stable technique is the displacement–pressure formulation ($\mathbf{u}$-p) with Q_1/P_0 discretisation. This method, commonly referred to as B-bar in the context of quasi-incompressible solids (or F-bar in the finite strains regime [3]), is based on the splitting of the deviatoric and volumetric components of the material response by introducing a piecewise discontinuous pressure degree of freedom [4]. Although it makes possible the resolution of problems involving incompressibility, the B-bar

*Corresponding author
Email addresses: rzorrilla@cimne.upc.edu (Rubén Zorrilla), rrossi@cimne.upc.edu (Riccardo Rossi), ramon.codina@upc.edu (Ramon Codina)

(and F-bar) technique is limited to quadrilateral (and hexahedral) meshes. In this regard, the Variational Multiscales Stabilisation (VMS) techniques [5] provide a general framework for the development of stable mixed formulations in presence of arbitrary and, in particular, equal-order interpolation pairs. This is exploited, among many other works, in [6] to implement a stable $\mathbf{u}$-p formulation with mixed Q_1/Q_1 and P_1/P_1 interpolation pairs. These works introduce a stress splitting into deviatoric and volumetric components, which are computed from the displacement and pressure nodal fields, respectively. While this bypasses the volumetric locking inconvenience, one cannot use standard strain-driven constitutive laws as these require the total strain to be computed. This limitation is overcome in [7] by replacing the pressure with the volumetric strain (ε^v) as nodal unknown, resulting in a $\mathbf{u}$-ε^v formulation capable to deal with (nearly) incompressible materials. As it is detailed in [7], the $\mathbf{u}$-ε^v formulation makes possible the usage of strain-driven material libraries with, possibly unstructured, low order meshes with a minimum computational overhead. Besides, it also overcomes the limitations of equal-order $\mathbf{u}$-p formulations when dealing with multi-material interfaces. Furthermore, we also note the displacement–strain ($\mathbf{u}$-$\boldsymbol{\varepsilon}$) and displacement–stress ($\mathbf{u}$-$\boldsymbol{\sigma}$) formulations presented in [8], the three field $\mathbf{u}$-$\boldsymbol{\sigma}$-p in [9, 10] and the $\mathbf{u}$-det($\mathbf{J}$) in [11], which introduces the determinant of the Jacobian as nodal unknown in order to extend the $\mathbf{u}$-ε^v to the finite strain regime. In case further details are needed, we refer the reader to [12] for an extremely detailed historical review on the numerical resolution of incompressible and nearly incompressible mechanical problems.

The extension of the previously discussed formulations to the dynamic regime might not be obvious as the kinematic/volumetric constraint likely has no evolution equation. For instance, in [13, 14] the authors address this by using an explicit time integration scheme in the context of $\mathbf{u}$-$\boldsymbol{\varepsilon}$ formulations. Another example can be found in [12], which introduces a rate equation for the pressure field evolution in $\mathbf{u}$-p problems. In this work, we aim to explore how the $\mathbf{u}$-ε^v formulation presented in [7] can be extended to consider transient problems. The approximation using finite differences is standard, and we only consider it as a reference in the numerical examples. We concentrate here in the modal analysis and in the associated (generalised) eigenvalue problem associated to it. When this problem is solved using classical residual-based VMS techniques, the original *linear* problem for the eigenvalue may be transformed into a *quadratic* problem for it at the discrete level. This issue is discussed in [15, 16], and may be overcome by using orthogonal sub-grid scales (see below), as we do in this paper.

The article is organized as follows: Section 2 describes the strong form, variational as well as the finite element discretisation and stabilisation of the problem to be solved; similarly, we do so for the eigenvalue problem in Section 3; Section 4 presents and discusses the algebraic forms resulting from Sections 2 and 3; in Section 5 we briefly describe the discrete modal analysis; the numerical experiments setup and results are detailed in Section 6; finally, the conclusions are summarised in Section 7.

2. Problem description

2.1. Strong form

The initial and boundary value problem we consider is solved for a time $t \in [0, T)$ on a computational domain $\Omega \subset \mathbb{R}^d$ ($d = 2, 3$), which boundary $\partial\Omega = \Gamma$ is defined from the Γ_D and Γ_N subsets as $\Gamma = \Gamma_D \cup \Gamma_N$ and $\Gamma_D \cap \Gamma_N = \emptyset$. Hence, the problem consists in finding the displacement field $\mathbf{u} : \Omega \times [0, T) \to \mathbb{R}^d$ and the volumetric strain field $\varepsilon^v : \Omega \times (0, T) \to \mathbb{R}$ such that

$$\rho\partial^2_{tt}\mathbf{u} - \nabla \cdot \boldsymbol{\sigma}(\boldsymbol{\varepsilon}) = \mathbf{f} \ \text{ in } \Omega,\ t \in (0, T)\ , \tag{1a}$$

$$\varepsilon^v - \nabla \cdot \mathbf{u} = 0 \ \text{ in } \Omega,\ t \in (0, T)\ , \tag{1b}$$

$$\mathbf{u} = \mathbf{0} \ \text{ on } \Gamma_D,\ t \in (0, T)\ , \tag{1c}$$

$$\mathbf{n} \cdot \boldsymbol{\sigma}(\boldsymbol{\varepsilon}) = \bar{\mathbf{t}} \ \text{ on } \Gamma_N,\ t \in (0, T)\ , \tag{1d}$$

$$\mathbf{u} = \mathbf{u}_0 \ \text{ in } \Omega,\ t = 0\ , \tag{1e}$$

$$\partial_t\mathbf{u} = \mathbf{v}_0 \ \text{ in } \Omega,\ t = 0\ . \tag{1f}$$

In previous equations, ∇ is the standard nabla operator while ρ and $\mathbf{f}$ are the known density and body force (e.g., gravity). $\mathbf{t}$ is the value of the surface traction to be imposed. Similarly, $\mathbf{u}_0$ and $\mathbf{v}_0$ are the displacement and velocity initial conditions. $\mathbf{n}$ is the unit vector normal to the corresponding boundary. $\boldsymbol{\sigma}$ denotes the Cauchy stress tensor,

which is obtained from the infinitesimal strain $\boldsymbol{\varepsilon}$. In this regard, this formulation stems from the splitting of $\boldsymbol{\varepsilon}$ in a deviatoric component and its volumetric counterpart. Hence, $\boldsymbol{\varepsilon}$ is defined as

$$\boldsymbol{\varepsilon} = \nabla^s \mathbf{u} - \frac{1}{\alpha}(\nabla \cdot \mathbf{u})\,\mathbf{I} + \frac{1}{\alpha}\varepsilon^v \mathbf{I}\,, \tag{2}$$

being $\mathbf{I}$ the second order identity tensor, ∇^s the symmetric gradient operator, and α a dimensional coefficient taken as $\alpha = d$ (i.e., 3 in the 3D case and 2 in the 2D plane strain and plane stress ones). The previous equation defines the strain splitting that enables the resolution of nearly incompressible materials. In this respect, we note that the the summation of the first two terms depending on $\mathbf{u}$ represent the deviatoric strain component while the last one depending on ε^v accounts for the volumetric one.

2.2. Weak form

As it is discussed in [7], a symmetric weak form for the problem in Eq. (1) can be obtained by introducing the strain splitting in Eq. (2) into the variational form of the $\mathbf{u}$-$\boldsymbol{\varepsilon}$ formulation [8]. To that purpose, let us first define the common notation $(\cdot,\cdot)$ for the L^2-inner product in Ω as well as $\langle\cdot,\cdot\rangle_R$ for the product of two functions in a region R. In conjunction, we also introduce the functional spaces $\mathbf{V} := \mathbf{H}^1_D(\Omega)$, i.e., the space of vector fields with components in H^1 vanishing on Γ_D, and $Q := L^2(\Omega)$, i.e., the space of square-integrable functions; these are the appropriate spaces for the displacement and volumetric strain approximations, respectively. Altogether, these allow us to define the weak form of the problem as find $\mathbf{u} : (0,T) \to \mathbf{V}$ and $\varepsilon^v : (0,T) \to Q$ such that

$$\rho\left(\mathbf{v}, \partial^2_{tt}\mathbf{u}\right) + (\nabla^s \mathbf{v}, \mathbb{C} : \nabla^s \mathbf{u}) + (\nabla\cdot\mathbf{v}, \kappa\varepsilon^v) - (\nabla\cdot\mathbf{v}, \kappa\nabla\cdot\mathbf{u}) = \langle \mathbf{v}, \mathbf{f}\rangle_\Omega + \langle \mathbf{v}, \mathbf{t}\rangle_{\Gamma_N}\,, \tag{3a}$$

$$(q, \kappa\varepsilon^v) - (q, \kappa\nabla\cdot\mathbf{u}) = 0\,, \tag{3b}$$

for all test functions $\mathbf{v} \in \mathbf{V}$ and $q \in Q$. We make clear that the introduction of the elasticity tensor $\mathbb{C}$ and the bulk modulus $\kappa := (\mathbf{I} : \mathbb{C} : \mathbf{I})/\alpha^2$ imply that as of now we are assuming an isotropic linear elastic constitutive behaviour, something strictly necessary for the modal analysis we target. Also note that κ is applied as a physical scaling parameter to Eq. (3b) We refer the reader to [7] for a detailed derivation of the weak form considering arbitrary stress-strain relations as well as for the special treatment of anisotropy. Likewise, it is also explained in this reference the interest of this formulation, in spite of the fact the the fully incompressible case $\kappa = \infty$ cannot be reached. In practice, the only limitation in the value of κ is the possible ill-conditioning of the final algebraic system.

Finally, let us observe that we can write

$$(\nabla^s \mathbf{v}, \mathbb{C} : \nabla^s \mathbf{u}) - (\nabla\cdot\mathbf{v}, \kappa\nabla\cdot\mathbf{u}) = (\nabla^s \mathbf{v}, \mathbb{C}_{\text{dev}} : \nabla^s \mathbf{u})\,,$$

where $\mathbb{C}_{\text{dev}}$ is the deviatoric elasticity tensor.

2.3. Finite element discretisation and stabilisation

First, we introduce the partition $\mathcal{T}_h = \{\Omega^k\}_{k=1}^{n_e}$ that divides the problem domain Ω into n_e finite elements of characteristic size h. Such partition allows one to construct the finite element spaces $\mathbf{V}_h$ and Q_h that approximate $\mathbf{V}$ and Q, respectively. In this work we only consider conforming and equal-order interpolations, meaning that the $\mathbf{u}$ and ε^v finite element approximations $\mathbf{u}_h$ and ε^v_h can be written as

$$\mathbf{u}(\mathbf{x}, t) \approx \mathbf{u}_h(\mathbf{x}, t) = \sum_{a=1}^{n_n} N_a(\mathbf{x})\mathbf{u}_a(t)$$

and

$$\varepsilon^v(\mathbf{x}, t) \approx \varepsilon^v_h(\mathbf{x}, t) = \sum_{a=1}^{n_n} N_a(\mathbf{x})\varepsilon^v_a(t)\,,$$

respectively. In the previous expressions, $N_a(\mathbf{x})$ denotes the nodal shape function of node a of the finite element partition, while $\mathbf{u}_a(t)$ and $\varepsilon^v_a(t)$ are the displacement and volumetric strain nodal values. The total number of nodes is n_n. Equivalently, the test functions $\mathbf{v}$ and q are approximated by $\mathbf{v}_h$ and q_h.

It is a known issue that using an equal-order interpolation pair in this sort of problem violates the inf-sup condition, and thus results in an unstable approximation that requires the introduction of any stabilisation technique. In this context, in this work we discuss two different approaches, both based on the VMS family of methods [5, 17]. The core of any VMS method is to split the solution fields as the summation of a finite element resolvable scale, in our case the previously defined $\mathbf{u}_h$ and ε_h^v, plus the so called subscales, which are to be modelled. Hence,

$$\mathbf{u} = \mathbf{u}_h + \mathbf{u}_s \ , \tag{4a}$$

$$\varepsilon^v = \varepsilon_h^v + \varepsilon_s^v \ , \tag{4b}$$

being $\mathbf{u}_s$ and ε_s^v the displacement and the volumetric strain subscales, which in the VMS methods we consider are defined from their corresponding finite element residuals; these are computed element-wise as

$$\mathbf{u}_s = \tau_{\mathbf{u}} P_s \left[\mathbf{f} - \rho \partial_{tt}^2 \mathbf{u}_h + \nabla \cdot \mathbb{C} : \nabla^s \mathbf{u}_h + \kappa \nabla \left(\varepsilon_h^v - \nabla \cdot \mathbf{u}_h \right) \right] \ , \tag{5a}$$

$$\varepsilon_s^v = \tau_{\varepsilon^v} P_s \left[\nabla \cdot \mathbf{u}_h - \varepsilon_h^v \right] \ , \tag{5b}$$

$\tau_{\mathbf{u}}$ and τ_{ε^v} are two stabilisation parameters defined as

$$\tau_{\mathbf{u}} = c_1 \frac{h^2}{\mu} \quad \text{and} \quad \tau_{\varepsilon^v} = c_2 \frac{\mu}{\mu + \kappa} \ . \tag{6}$$

μ is the second Lamé parameter (i.e., the shear modulus G) while c_1 and c_2 are two algorithmic constants that we will define later on. P_s is the projection operator onto the space of the sub-grid scales of either $\mathbf{u}_s$ or ε_s^v.

Introducing the solution splitting (Eq. (4) together with the sub-grid scales definition (Eq. (5)) into the variational form (Eq. (3)) results in

$$\begin{aligned} &\rho \left(\mathbf{v}_h, \partial_{tt}^2 \mathbf{u}_h \right) + \rho \left(\mathbf{v}_h, \partial_{tt}^2 \mathbf{u}_s \right) + \left(\nabla^s \mathbf{v}_h, \mathbb{C} : \nabla^s \mathbf{u}_h \right) - \sum_k \langle \nabla \cdot (\mathbb{C} : \nabla^s \mathbf{v}_h), \mathbf{u}_s \rangle_{\Omega^k} + \left(\nabla \cdot \mathbf{v}_h, \kappa \varepsilon_h^v \right) \\ &\quad + \sum_k \langle \kappa \nabla \cdot \mathbf{v}_h, \varepsilon_s^v \rangle_{\Omega^k} - \left(\nabla \cdot \mathbf{v}_h, \kappa \nabla \cdot \mathbf{u}_h \right) + \sum_k \langle \kappa \nabla (\nabla \cdot \mathbf{v}_h), \mathbf{u}_s \rangle_{\Omega^k} = \langle \mathbf{v}_h, \mathbf{f} \rangle_\Omega + \langle \mathbf{v}_h, \mathbf{t} \rangle_{\Gamma_N} \end{aligned} \tag{7a}$$

$$\left(q_h, \kappa \varepsilon_h^v \right) + \sum_k \langle \kappa q_h, \varepsilon_s^v \rangle_{\Omega^k} - \left(q_h, \kappa \nabla \cdot \mathbf{u}_h \right) + \sum_k \langle \kappa \nabla q_h, \mathbf{u}_s \rangle_{\Omega^k} = 0 \ , \tag{7b}$$

to which we have already applied the required integration by parts as well as introduced the assumption that the sub-grid scales vanish over the element boundaries. By further assuming that the sub-grid scales transient behaviour can be neglected (i.e., $\partial_{tt}^s \mathbf{u}_s \approx \mathbf{0}$) and dropping all the second-order derivatives, as we will only consider first-order finite element interpolations, we obtain the final stabilised variational form, which already includes the sub-grid scales definition in Eq. (5). Hence, the problem is find $\mathbf{u}_h \in \mathbf{V}_h$ and $\varepsilon_h^v \in Q_h$ such that

$$\begin{aligned} &\rho \left(\mathbf{v}_h, \partial_{tt}^2 \mathbf{u}_h \right) + \left(\nabla^s \mathbf{v}_h, \mathbb{C} : \nabla^s \mathbf{u}_h \right) + \left(\nabla \cdot \mathbf{v}_h, \kappa \varepsilon_h^v \right) - \left(\nabla \cdot \mathbf{v}_h, \kappa \nabla \cdot \mathbf{u}_h \right) \\ &\qquad + \sum_k \langle \kappa \nabla \cdot \mathbf{v}_h, \tau_{\varepsilon^v} P_s \left[\nabla \cdot \mathbf{u}_h - \varepsilon_h^v \right] \rangle_{\Omega^k} = \langle \mathbf{v}_h, \mathbf{f} \rangle_\Omega + \langle \mathbf{v}_h, \mathbf{t} \rangle_{\Gamma_N} \end{aligned} \tag{8a}$$

$$\left(q_h, \kappa \varepsilon_h^v \right) - \left(q_h, \kappa \nabla \cdot \mathbf{u}_h \right) + \sum_k \langle \kappa q_h, \tau_{\varepsilon^v} P_s \left[\nabla \cdot \mathbf{u}_h - \varepsilon_h^v \right] \rangle_{\Omega^k} + \sum_k \langle \kappa \nabla q_h, \tau_{\mathbf{u}} P_s \left[\mathbf{f} - \rho \partial_{tt}^2 \mathbf{u}_h + \kappa \nabla \varepsilon_h^v \right] \rangle_{\Omega^k} = 0 \ , \tag{8b}$$

for all $\mathbf{v}_h \in \mathbf{V}_h$ and $q_h \in Q_h$.

The method is completed with the selection of the projection operator P_s, which ultimately defines the space for the subscales. One option is to assume that the sub-grid scale space is that of their corresponding finite element residuals, meaning that $P_s = I$ (the identity) and leading to the so called Algebraic Sub-Grid Scales (ASGS) approach [7]. The other option is to take the sub-grid scales from the space that is L^2-orthogonal to the finite element one. In this case P_s is the orthogonal projection to this space (i.e., $P_s = P_h^\perp$) and the method is called Orthogonal Sub-Grid Scales (OSGS) [18]. Though both options have been proved to work in similar problems, the OSGS has some superior theoretical and practical advantages [8, 18, 19]. Specifically, and as we will detail later on, the use of the OSGS approach becomes crucial for the modal analysis effectiveness.

3. Eigenvalue problem arising in modal analysis

3.1. Strong form

The modal analysis consists of expanding the unknowns of the problem in Eq. (1) in terms of the modes associated to the homogeneous problem, that is, considering $\mathbf{f} = \mathbf{0}$ and $\bar{\mathbf{t}} = \mathbf{0}$. These modes are the amplitudes in the Fourier expansion of the displacement solution of the homogeneous problem as

$$\mathbf{u}_H(\mathbf{x}, t) = \sum_{n=0}^{\infty} e^{i\omega_n t} \boldsymbol{\phi}_n(\mathbf{x}) \, ,$$

and the volumetric strain ε^v as

$$\varepsilon^v_H(\mathbf{x}, t) = \sum_{n=0}^{\infty} e^{i\omega_n t} \psi_n(\mathbf{x}) \, .$$

The frequencies ω_n (the same for $\mathbf{u}_H$ and ε^v_H) and the amplitudes $\boldsymbol{\phi}_n$, ψ_n, $n = 0, 1, 2, \ldots$, are solution of the eigenvalue problem that is obtained by imposing that $\mathbf{u}_H(\mathbf{x}, t)$ and $\varepsilon^v_H(\mathbf{x}, t)$ are solution of

$$\begin{aligned}
\rho \partial^2_{tt} \mathbf{u}_H - \nabla \cdot (\mathbb{C} : \nabla^s \mathbf{u}_H) + \kappa \nabla (\nabla \cdot \mathbf{u}_H - \varepsilon^v_H) = \mathbf{0} \;\; &\text{in } \Omega, \; t \in (0, T) \, , \\
\varepsilon^v_H - \nabla \cdot \mathbf{u}_H = 0 \;\; &\text{in } \Omega, \; t \in (0, T) \, , \\
\mathbf{u}_H = \mathbf{0} \;\; &\text{on } \Gamma_D, \; t \in (0, T) \, , \\
\mathbf{n} \cdot (\mathbb{C} : \nabla^s \mathbf{u}_H) - \kappa (\nabla \cdot \mathbf{u}_H - \varepsilon^v_H) \mathbf{n} = \mathbf{0} \;\; &\text{on } \Gamma_N, \; t \in (0, T) \, , \\
\mathbf{u}_H = \mathbf{u}_0 \;\; &\text{in } \Omega, \; t = 0 \, , \\
\partial_t \mathbf{u}_H = \mathbf{v}_0 \;\; &\text{in } \Omega, \; t = 0 \, .
\end{aligned}$$

Assuming the modes to be linearly independent (as it can be checked a posteriori) this leads to the generalised eigenvalue problem (GEVP):

$$-\nabla \cdot (\mathbb{C} : \nabla^s \boldsymbol{\phi}_n) + \kappa \nabla (\nabla \cdot \boldsymbol{\phi}_n - \psi_n) = \rho \omega_n^2 \boldsymbol{\phi}_n \;\; \text{in } \Omega \, , \tag{10a}$$

$$\psi_n - \nabla \cdot \boldsymbol{\phi}_n = 0 \;\; \text{in } \Omega \, , \tag{10b}$$

$$\boldsymbol{\phi}_n = \mathbf{0} \;\; \text{on } \Gamma_D \, , \tag{10c}$$

$$\mathbf{n} \cdot (\mathbb{C} : \nabla^s \boldsymbol{\phi}_n) - \kappa (\nabla \cdot \boldsymbol{\phi}_n - \psi_n) \mathbf{n} = \mathbf{0} \;\; \text{on } \Gamma_N \, , \tag{10d}$$

for $n = 1, 2, \ldots$. Hence, solving the GEVP results in a complete set of eigenpairs, which can be arranged as

$$[\boldsymbol{\phi}_1(\mathbf{x}), \boldsymbol{\phi}_2(\mathbf{x}), \ldots, \boldsymbol{\phi}_n(\mathbf{x}), \ldots] \, , \quad [\psi_1(\mathbf{x}), \psi_2(\mathbf{x}), \ldots, \psi_n(\mathbf{x}), \ldots] \quad \text{and} \quad 0 < \omega_1^2 \leq \omega_2^2 \leq \ldots \omega_n^2 \leq \ldots \, .$$

The operator $-\nabla \cdot (\mathbb{C} : \nabla^s(\cdot)) + \kappa \nabla (\nabla \cdot (\cdot)) = -\nabla \cdot (\mathbb{C}_{\text{dev}} : \nabla^s(\cdot))$ is symmetric and positive-semidefinite. This allows one to prove that for all $i = 0, 1, 2, \ldots$ the eigenvalues ω_i^2 are indeed positive and the eigenvectors $\boldsymbol{\phi}_i$ can be taken as an L^2 orthogonal set (and therefore indeed linearly independent) and also orthogonal with respect to the inner product induced by $-\nabla \cdot (\mathbb{C}_{\text{dev}} : \nabla^s(\cdot))$. Any normalisation to make them unique can be chosen.

At this point, it is clear that each of the eigenfunctions $\boldsymbol{\phi}_n$, ψ_n and eigenvalues ω_n correspond to a particular mode n of the decomposition. Hence, and for the sake of a lightweight notation, in what follows we will omit the subindex n when referring to any of these.

3.2. Weak form

The stable discrete form of the eigenvalue problem is derived similar to the mixed $\mathbf{u}$-ε^v one (Eq. (8)). Therefore, we retake the previously defined notation and functional spaces $\mathbf{V}$ and Q to define the weak form of the GEVP (Eq. (10)) as find $\boldsymbol{\phi} \in \mathbf{V}$, $\psi \in Q$ and $\omega^2 \in \mathbb{R}^+$ such that

$$(\nabla^s \mathbf{v}, \mathbb{C} : \nabla^s \boldsymbol{\phi}) + (\nabla \cdot \mathbf{v}, \kappa \psi) - (\nabla \cdot \mathbf{v}, \kappa \nabla \cdot \boldsymbol{\phi}) = \rho \omega^2 (\mathbf{v}, \boldsymbol{\phi}) \, , \tag{11a}$$

$$(q, \kappa \psi) - (q, \kappa \nabla \cdot \boldsymbol{\phi}) = 0 \, , \tag{11b}$$

for all test functions $\mathbf{v} \in \mathbf{V}$ and $q \in Q$. Note that, as we did in Eq. (3b), we introduce κ as a scaling physical parameter to Eq. (11b).

3.3. Finite element discretisation and stabilisation

As previously mentioned, in this work we only consider equal-order finite element interpolation pairs, unstable for the standard Galerkin approximation. Therefore, we discretise the $\boldsymbol{\phi}(\mathbf{x})$ and $\psi(\mathbf{x})$ eigenfunctions using a linear conforming finite element approximation as

$$\boldsymbol{\phi}(\mathbf{x}) \approx \boldsymbol{\phi}_h(\mathbf{x}) = \sum_{a=1}^{n_n} N_a(\mathbf{x})\boldsymbol{\phi}_a$$

and

$$\psi(\mathbf{x}) \approx \psi_h(\mathbf{x}) = \sum_{a=1}^{n_n} N_a(\mathbf{x})\psi_a \ ,$$

respectively. Furthermore, we also introduce the VMS-based solution splitting for the eigenfunctions, that is

$$\boldsymbol{\phi} = \boldsymbol{\phi}_h + \boldsymbol{\phi}_s \ , \tag{12a}$$

$$\psi = \psi_h + \psi_s \ . \tag{12b}$$

Similar to what is done for the $\mathbf{u}_s$ and ε^v_s, the $\boldsymbol{\phi}_s$ and ψ_s eigenfunctions sub-grid scales are defined from their corresponding finite element residuals as

$$\boldsymbol{\phi}_s = \tau_{\mathbf{u}} P_s \left[\rho\omega_h^2\boldsymbol{\phi}_h + \nabla\cdot\mathbb{C} : \nabla^s\boldsymbol{\phi}_h + \kappa\nabla\left(\psi_h - \nabla\cdot\boldsymbol{\phi}_h\right)\right] \ , \tag{13a}$$

$$\psi_s = \tau_{\varepsilon^v} P_s \left[\nabla\cdot\boldsymbol{\phi}_h - \psi_h\right] \ , \tag{13b}$$

being $\tau_{\mathbf{u}}$, τ_{ε^v} and P_s the previously defined stabilisation parameters (Eq. (6)) and projection operator.

Introducing the sub-grid scales separation in Eq. (12) into the variational form in Eq. (11) results in the GEVP stabilised functional

$$\begin{aligned} -\rho\omega_h^2\left(\mathbf{v}_h, \boldsymbol{\phi}_h\right) - \rho\omega_h^2\left(\mathbf{v}_h, \boldsymbol{\phi}_s\right) + \left(\nabla^s\mathbf{v}_h, \mathbb{C} : \nabla^s\boldsymbol{\phi}_h\right) - \sum_k \langle\nabla\cdot\left(\mathbb{C} : \nabla^s\mathbf{v}_h\right), \boldsymbol{\phi}_s\rangle_{\Omega^k} \\ + \left(\nabla\cdot\mathbf{v}_h, \kappa\psi_h\right) + \sum_k \langle\kappa\nabla\cdot\mathbf{v}_h, \psi_s\rangle_{\Omega^k} - \left(\nabla\cdot\mathbf{v}_h, \kappa\nabla\cdot\boldsymbol{\phi}_h\right) + \sum_k \langle\kappa\nabla(\nabla\cdot\mathbf{v}_h), \boldsymbol{\phi}_s\rangle_{\Omega^k} = \mathbf{0} \ , \end{aligned} \tag{14a}$$

$$\left(q_h, \kappa\psi_h\right) + \sum_k \langle\kappa q_h, \psi_s\rangle_{\Omega^k} - \left(q_h, \kappa\nabla\cdot\boldsymbol{\phi}_h\right) + \sum_k \langle\kappa\nabla q_h, \boldsymbol{\phi}_s\rangle_{\Omega^k} = 0 \ , \tag{14b}$$

which already includes the required integration by parts. Lastly, we insert the $\boldsymbol{\phi}_s$ and ψ_s expression from Eq. (13) and drop the higher order derivatives to obtain the final form to be implemented, which reads as: find $\boldsymbol{\phi}_h \in \mathbf{V}_h$ and $\psi_h \in Q_h$ such that

$$\begin{aligned} -\rho\omega_h^2\left(\mathbf{v}_h, \boldsymbol{\phi}_h\right) + \left(\nabla^s\mathbf{v}_h, \mathbb{C} : \nabla^s\boldsymbol{\phi}_h\right) + \left(\nabla\cdot\mathbf{v}_h, \kappa\psi_h\right) - \left(\nabla\cdot\mathbf{v}_h, \kappa\nabla\cdot\boldsymbol{\phi}_h\right) \\ - \rho\omega_h^2 \sum_k \langle\mathbf{v}_h, \tau_{\mathbf{u}} P_s\left[\rho\omega_h^2\boldsymbol{\phi}_h + \kappa\nabla\psi_h\right]\rangle_{\Omega^k} + \sum_k \langle\kappa\nabla\cdot\mathbf{v}_h, \tau_{\varepsilon^v} P_s\left[\nabla\cdot\boldsymbol{\phi}_h - \psi_h\right]\rangle_{\Omega^k} = \mathbf{0} \ , \end{aligned} \tag{15a}$$

$$\left(q_h, \kappa\psi_h\right) - \left(q_h, \kappa\nabla\cdot\boldsymbol{\phi}_h\right) + \sum_k \langle\kappa q_h, \tau_{\varepsilon^v} P_s\left[\nabla\cdot\boldsymbol{\phi}_h - \psi_h\right]\rangle_{\Omega^k} + \sum_k \langle\kappa\nabla q_h, \tau_{\mathbf{u}} P_s\left[\rho\omega_h^2\boldsymbol{\phi}_h + \kappa\nabla\psi_h\right]\rangle_{\Omega^k} = 0 \ . \tag{15b}$$

for all $\mathbf{v}_h \in \mathbf{V}_h$ and $q_h \in Q_h$.

At this point, it becomes apparent that the projection P_s determines the problem in Eq. (15). Specifically, we note that in general $P_s\left[\boldsymbol{\phi}_h\right] \neq \mathbf{0}$. In consequence, the first stabilisation term in Eq. (15a) results in an ω_h^4 contribution, that is to say, in a quadratic (nonlinear) GEVP. The most immediate solution for such inconvenience is to choose $P_s = P_h^\perp$, that is to say, using the OSGS approach, since $P_h^\perp\left[\boldsymbol{\phi}_h\right] = \mathbf{0}$. This fact is elaborated in [15, 16].

Remark 1. Even though we have not undertaken the convergence analysis of this eigenvalue problem, the expected order of convergence in h of the displacement field eigenvectors is p in the norm of $H^1(\Omega)$ (i.e., the norm of $\mathbf{V}$), p being here the polynomial order of the finite element space. Thus, the expected order of convergence of the eigenvalues is $2p$. This is obviously true if the continuous displacement field eigenvectors belong to $H^{p+1}(\Omega)$. As shall be reported in Section 6, convergence rates smaller that $2p$ are found if this does not happen. In this work we are interested in the case $p = 1$.

4. Algebraic form

In this section we discuss the algebraic (matrix) forms resulting from the previously defined variational problems. As we pinpointed before, the selection of the stabilisation approach (i.e., ASGS or OSGS) becomes crucial for the resulting algebraic problem. Hence, we start by discussing the most simple case, which is the model problem (Eq. (8)) with ASGS stabilisation, that is taking $P_s = I$. For the sake of simplifying the discussion at hand, let us also denote the mass and stiffness matrices as $\mathbf{M}$ and $\mathbf{K}$, respectively. We also define the vectors $\mathbf{U}$ and $\boldsymbol{\mathcal{E}}^v$ to collect the $\mathbf{u}_h$ and ε_h^v unknown nodal values as well as $\mathbf{F}$ to do so for the external forces (i.e., loads). Using the customary dot notation for the time derivatives, this allows us to write the algebraic ASGS version of the problem in Eq. (8) as

$$\begin{bmatrix} \mathbf{M}_{\mathbf{uu}} & \mathbf{0} \\ \mathbf{M}_{\varepsilon^v\mathbf{u}} & \mathbf{0} \end{bmatrix} \begin{bmatrix} \ddot{\mathbf{U}} \\ \ddot{\boldsymbol{\mathcal{E}}}^v \end{bmatrix} + \begin{bmatrix} \mathbf{K}_{\mathbf{uu}} & \mathbf{K}_{\mathbf{u}\varepsilon^v} \\ \mathbf{K}_{\varepsilon^v\mathbf{u}} & \mathbf{K}_{\varepsilon^v\varepsilon^v} \end{bmatrix} \begin{bmatrix} \mathbf{U} \\ \boldsymbol{\mathcal{E}}^v \end{bmatrix} = \begin{bmatrix} \mathbf{F} \\ \mathbf{0} \end{bmatrix} . \tag{16}$$

As discussed in [7], the ASGS variational form yields a symmetric stiffness matrix (i.e., $\mathbf{K}_{\mathbf{u}\varepsilon^v} = \mathbf{K}^T_{\varepsilon^v\mathbf{u}}$). However, it can be clearly observed that the dynamic problem is no longer symmetric after the appearance of the $\mathbf{M}_{\varepsilon^v\mathbf{u}}$ component in the mass matrix. This inconvenience can be readily fixed by introducing the OSGS approach. In this regard, we note that the discrete orthogonal projection $P_h^\perp$ can be implemented as $P_h^\perp = I - P_{L^2}$, being P_{L^2} the customary discrete L^2-projection. Hence, the algebraic OSGS version of the problem in Eq. (8) is

$$\begin{bmatrix} \mathbf{M}_{\mathbf{uu}} & \mathbf{0} & \mathbf{0} & \mathbf{0} \\ \mathbf{0} & \mathbf{0} & \mathbf{0} & \mathbf{0} \\ \mathbf{0} & \mathbf{0} & \mathbf{0} & \mathbf{0} \\ \mathbf{0} & \mathbf{0} & \mathbf{0} & \mathbf{0} \end{bmatrix} \begin{bmatrix} \ddot{\mathbf{U}} \\ \ddot{\boldsymbol{\mathcal{E}}}^v \\ \ddot{\boldsymbol{\Pi}}_{\mathbf{u}} \\ \ddot{\boldsymbol{\Pi}}_{\varepsilon^v} \end{bmatrix} + \begin{bmatrix} \mathbf{K}_{\mathbf{uu}} & \mathbf{K}_{\mathbf{u}\varepsilon^v} & \mathbf{0} & \mathbf{K}_{\mathbf{u}\boldsymbol{\Pi}_{\mathbf{u}}} \\ \mathbf{K}_{\varepsilon^v\mathbf{u}} & \mathbf{K}_{\varepsilon^v\varepsilon^v} & \mathbf{K}_{\varepsilon^v\boldsymbol{\Pi}_{\mathbf{u}}} & \mathbf{K}_{\varepsilon^v\boldsymbol{\Pi}_{\varepsilon^v}} \\ \mathbf{0} & \mathbf{K}_{\boldsymbol{\Pi}_{\mathbf{u}}\varepsilon^v} & \mathbf{K}_{\boldsymbol{\Pi}_{\mathbf{u}}\boldsymbol{\Pi}_{\mathbf{u}}} & \mathbf{0} \\ \mathbf{K}_{\boldsymbol{\Pi}_{\varepsilon^v}\mathbf{u}} & \mathbf{K}_{\boldsymbol{\Pi}_{\varepsilon^v}\varepsilon^v} & \mathbf{0} & \mathbf{K}_{\boldsymbol{\Pi}_{\varepsilon^v}\boldsymbol{\Pi}_{\varepsilon^v}} \end{bmatrix} \begin{bmatrix} \mathbf{U} \\ \boldsymbol{\mathcal{E}}^v \\ \boldsymbol{\Pi}_{\mathbf{u}} \\ \boldsymbol{\Pi}_{\varepsilon^v} \end{bmatrix} = \begin{bmatrix} \mathbf{F} \\ \mathbf{0} \\ \mathbf{0} \\ \mathbf{0} \end{bmatrix} . \tag{17}$$

Comparing to the ASGS version of the problem (Eq. (16)), one can notice the introduction of $\boldsymbol{\Pi}_{\mathbf{u}}$ and $\boldsymbol{\Pi}_{\varepsilon^v}$ as nodal unknowns. These are the vectors collecting the nodal values of the finite element residual L^2-projections (see the sub-grid scales definitions in Eq. (5)). Concerning the projection, and considering that we are interested in low order elements, we opt for the lumped L^2-projection, as it can be guessed from the diagonal nature of the $\mathbf{K}_{\boldsymbol{\Pi}_\bullet\boldsymbol{\Pi}_\bullet}$ block. In this regard, we shall mention that preliminary experiments reported no clear advantage on doing the consistent L^2-projection (which could be necessary for higher order interpolations). Taking this into consideration, we decide to keep the lumped version for the sake of having a better conditioned system.

By inspecting Eq. (17) one can easily note that $\mathbf{M}_{\varepsilon^v\mathbf{u}} = \mathbf{0}$, meaning that the OSGS is able to recover the mass matrix symmetry. This comes after the fact that $P_h^\perp[\partial_{tt}^2\mathbf{u}_h] = \mathbf{0}$. Besides, the OSGS stiffness matrix can be easily symmetrized by scaling the rows corresponding to $\boldsymbol{\Pi}_{\mathbf{u}}$ and $\boldsymbol{\Pi}_{\varepsilon^v}$ by $\tau_{\mathbf{u}}$ and $\kappa\tau_{\varepsilon^v}$, respectively. In short, the OSGS approach makes possible to extend the problem to the dynamic case while keeping the symmetry of its static counterpart. This is important both for theoretical and for practical reasons. Regarding the former, the spectral theorem applies, thus guaranteeing that the eigenvalues are real (and positive); concerning the latter, tailored and more efficient numerical linear algebra solvers can be used.

Similarly, we define the vectors $\boldsymbol{\Phi}$ and $\boldsymbol{\Psi}$ to collect the $\boldsymbol{\phi}_h$ and ψ_h unknown nodal values. Hence, the algebraic form of the ASGS-stabilised eigenvalue problem (Eq. (15)) can be written as

$$\begin{bmatrix} \mathbf{K}_{\boldsymbol{\phi}\boldsymbol{\phi}} & \mathbf{K}_{\boldsymbol{\phi}\psi} \\ \mathbf{K}_{\psi\boldsymbol{\phi}} & \mathbf{K}_{\psi\psi} \end{bmatrix} \begin{bmatrix} \boldsymbol{\Phi} \\ \boldsymbol{\Psi} \end{bmatrix} = \lambda_h \begin{bmatrix} \mathbf{M}_{\boldsymbol{\phi}\boldsymbol{\phi}} & \mathbf{M}_{\boldsymbol{\phi}\psi} \\ \mathbf{M}_{\psi\boldsymbol{\phi}} & \mathbf{0} \end{bmatrix} \begin{bmatrix} \boldsymbol{\Phi} \\ \boldsymbol{\Psi} \end{bmatrix} + \lambda_h^2 \begin{bmatrix} \mathbf{M}^*_{\boldsymbol{\phi}\boldsymbol{\phi}} & \mathbf{0} \\ \mathbf{0} & \mathbf{0} \end{bmatrix} \begin{bmatrix} \boldsymbol{\Phi} \\ \boldsymbol{\Psi} \end{bmatrix} , \tag{18}$$

being $\lambda_h = \omega_h^2$. Eq. (18) reveals that the ASGS approach results in a nonlinear generalised eigenproblem As previously mentioned, such inconvenience can be bypassed by using the OSGS as $P_h^\perp[\boldsymbol{\phi}_h] = \mathbf{0}$ yields $\mathbf{M}^*_{\boldsymbol{\phi}\boldsymbol{\phi}} = \mathbf{0}$. Therefore, introducing $\boldsymbol{\Pi}_{\boldsymbol{\phi}}$ and $\boldsymbol{\Pi}_{\psi}$ to collect the corresponding L^2-projection nodal values allows to write the OSGS GEVP as

$$\begin{bmatrix} \mathbf{K}_{\boldsymbol{\phi}\boldsymbol{\phi}} & \mathbf{K}_{\boldsymbol{\phi}\psi} & \mathbf{0} & \mathbf{K}_{\boldsymbol{\phi}\boldsymbol{\Pi}_{\boldsymbol{\phi}}} \\ \mathbf{K}_{\psi\boldsymbol{\phi}} & \mathbf{K}_{\psi\psi} & \mathbf{K}_{\psi\boldsymbol{\Pi}_{\boldsymbol{\phi}}} & \mathbf{K}_{\psi\boldsymbol{\Pi}_{\psi}} \\ \mathbf{0} & \mathbf{K}_{\boldsymbol{\Pi}_{\boldsymbol{\phi}}\psi} & \mathbf{K}_{\boldsymbol{\Pi}_{\boldsymbol{\phi}}\boldsymbol{\Pi}_{\boldsymbol{\phi}}} & \mathbf{0} \\ \mathbf{K}_{\boldsymbol{\Pi}_{\psi}\boldsymbol{\phi}} & \mathbf{K}_{\boldsymbol{\Pi}_{\psi}\psi} & \mathbf{0} & \mathbf{K}_{\boldsymbol{\Pi}_{\psi}\boldsymbol{\Pi}_{\psi}} \end{bmatrix} \begin{bmatrix} \boldsymbol{\Phi} \\ \boldsymbol{\Psi} \\ \boldsymbol{\Pi}_{\boldsymbol{\phi}} \\ \boldsymbol{\Pi}_{\psi} \end{bmatrix} = \lambda_h \begin{bmatrix} \mathbf{M}_{\boldsymbol{\phi}\boldsymbol{\phi}} & \mathbf{0} & \mathbf{0} & \mathbf{0} \\ \mathbf{0} & \mathbf{0} & \mathbf{0} & \mathbf{0} \\ \mathbf{0} & \mathbf{0} & \mathbf{0} & \mathbf{0} \\ \mathbf{0} & \mathbf{0} & \mathbf{0} & \mathbf{0} \end{bmatrix} \begin{bmatrix} \boldsymbol{\Phi} \\ \boldsymbol{\Psi} \\ \boldsymbol{\Pi}_{\boldsymbol{\phi}} \\ \boldsymbol{\Pi}_{\psi} \end{bmatrix} . \tag{19}$$

Besides being symmetric, something that enables the use of efficient sparse iterative eigenvalue solvers, the stiffness and mass matrices of the dynamic (Eq. (17)) and the eigenvalue (Eq. (19)) OSGS problems are identical, thus resulting in a much more clean and convenient code implementation.

Finally, we note that it is convenient to solve the GEVP for the Schur complement of the block corresponding to $\boldsymbol{\Psi}$, $\boldsymbol{\Pi}_{\boldsymbol{\phi}}$ and $\boldsymbol{\Pi}_{\psi}$, which we denote as $\mathbf{S}$, rather than for the complete form in Eq. (19). Hence, we define the Schur complement $\mathbf{K}/\mathbf{S}$ as

$$\mathbf{K}_S := \mathbf{K}/\mathbf{S} = \mathbf{K}_{\mathbf{uu}} - \begin{bmatrix} \mathbf{K}_{\mathbf{u}\varepsilon^v} & \mathbf{0} & \mathbf{K}_{\mathbf{u}\Pi_{\mathbf{u}}} \end{bmatrix} \begin{bmatrix} \mathbf{K}_{\varepsilon^v\varepsilon^v} & \mathbf{K}_{\varepsilon^v\Pi_{\mathbf{u}}} & \mathbf{K}_{\varepsilon^v\Pi_{\varepsilon^v}} \\ \mathbf{K}_{\Pi_{\mathbf{u}}\varepsilon^v} & \mathbf{K}_{\Pi_{\mathbf{u}}\Pi_{\mathbf{u}}} & \mathbf{0} \\ \mathbf{K}_{\Pi_{\varepsilon^v}\varepsilon^v} & \mathbf{0} & \mathbf{K}_{\Pi_{\varepsilon^v}\Pi_{\varepsilon^v}} \end{bmatrix}^{-1} \begin{bmatrix} \mathbf{K}_{\varepsilon^v\mathbf{u}} \\ \mathbf{0} \\ \mathbf{K}_{\Pi_{\varepsilon^v}\mathbf{u}} \end{bmatrix} , \tag{20}$$

which results in the statically condensed GEVP

$$\mathbf{K}_S \boldsymbol{\Phi} = \lambda_h \mathbf{M}_{\boldsymbol{\phi}\boldsymbol{\phi}} \boldsymbol{\Phi} . \tag{21}$$

Similarly, the linear system in Eq. (17) can be statically condensed as

$$\mathbf{M}_{\mathbf{uu}} \ddot{\mathbf{U}} + \mathbf{K}_S \mathbf{U} = \mathbf{F} . \tag{22}$$

It is important to highlight the symmetry of block $\mathbf{S}$, which makes possible to implement the statically condensed problem(s) as a linear operator leveraging fast iterative solvers for sparse Hermitian matrices.

Remark 2. Though Eq. (17) introduces the L^2-projection nodal values as an unknown, these can be treated iteratively by using a block-Gauss-Seidel scheme for $\mathbf{U}$-$\boldsymbol{\mathcal{E}}^v$ on the one side and $\boldsymbol{\Pi}_{\mathbf{u}}$-$\boldsymbol{\Pi}_{\varepsilon^v}$ on the other. This would allow the OSGS problem to keep the ASGS number of degrees of freedom. However, for the eigenvalue problem this iterative treatment of the projection would require acting on the numerical eigenvalue solver, loosing the convenience of employing this solver as a black-box. Furthermore, even though we have not explored this, the iterative scheme employed to deal with the projections (e.g., Gauss-Seidel) could be coupled with the iterative scheme to compute the eigensolution of the problem.

Remark 3. The nonlinear GEVP in Eq. (18) can be rewritten as

$$\mathbf{K}'\mathbf{z} = \lambda_h \mathbf{M}'\mathbf{z}$$

by introducing the modified eigenvector $\mathbf{z}^T = [\lambda_h\boldsymbol{\Phi}, \lambda_h\boldsymbol{\Psi}, \boldsymbol{\Phi}, \boldsymbol{\Psi}]$ as well as the corresponding modified stiffness and mass matrices $\mathbf{K}'$ and $\mathbf{M}'$. Hence, the modified problem is

$$\begin{bmatrix} \mathbf{I} & \mathbf{0} & \mathbf{0} & \mathbf{0} \\ \mathbf{0} & \mathbf{I} & \mathbf{0} & \mathbf{0} \\ -\mathbf{M}_{\boldsymbol{\phi}\boldsymbol{\phi}} & -\mathbf{M}_{\boldsymbol{\phi}\psi} & \mathbf{K}_{\boldsymbol{\phi}\boldsymbol{\phi}} & \mathbf{K}_{\boldsymbol{\phi}\psi} \\ -\mathbf{M}_{\psi\boldsymbol{\phi}} & \mathbf{0} & \mathbf{K}_{\psi\boldsymbol{\phi}} & \mathbf{K}_{\psi\psi} \end{bmatrix} \begin{bmatrix} \lambda_h\boldsymbol{\Phi} \\ \lambda_h\boldsymbol{\Psi} \\ \boldsymbol{\Phi} \\ \boldsymbol{\Psi} \end{bmatrix} = \lambda_h \begin{bmatrix} \mathbf{0} & \mathbf{0} & \mathbf{I} & \mathbf{0} \\ \mathbf{0} & \mathbf{0} & \mathbf{0} & \mathbf{I} \\ \mathbf{0} & \mathbf{0} & \mathbf{M}^*_{\boldsymbol{\phi}\boldsymbol{\phi}} & \mathbf{0} \\ \mathbf{0} & \mathbf{0} & \mathbf{0} & \mathbf{0} \end{bmatrix} \begin{bmatrix} \lambda_h\boldsymbol{\Phi} \\ \lambda_h\boldsymbol{\Psi} \\ \boldsymbol{\Phi} \\ \boldsymbol{\Psi} \end{bmatrix} .$$

As it can be noted, the resulting matrix $\mathbf{K}'$ is not symmetric, and thus precludes the use of standard sparse iterative eigenvalue solvers.

5. Modal analysis

The eigenvalues and eigenvectors resulting from the solving the GEVP can be used as a basis to alternatively express the dynamic problem solution. Hence, the displacement time evolution can be written as

$$\mathbf{U}(t) = \sum_{i=1}^{n} z_i(t) \boldsymbol{\Phi}_i , \tag{23}$$

with $z_i(t)$ being appropriate scalar functions to be determined. In the structural mechanics context, $\boldsymbol{\Phi}_i$ is commonly referred to as the ith-mode of vibration (or simply ith-mode) while z_i is the corresponding amplitude of that mode.

Taking all the decomposition modes makes Eq. (23) exact. However, taking m modes such that $m < n$ makes possible to build the approximation to the problem solution

$$\mathbf{U}(t) \approx \tilde{\mathbf{U}}(t) = \sum_{i=1}^{m} z_i(t)\boldsymbol{\Phi}_i \ . \tag{24}$$

Such approximation can be written in matrix form as

$$\tilde{\mathbf{U}} = \boldsymbol{\Xi}\mathbf{Z} \ .$$

$\boldsymbol{\Xi}$ and $\mathbf{Z}$ are the arrays storing the m-modes of the approximation and their corresponding amplitudes, respectively. Hence, these are defined as

$$\boldsymbol{\Xi} := \begin{bmatrix} \boldsymbol{\Phi}_1 & \dots & \boldsymbol{\Phi}_m \end{bmatrix} \in \mathbb{R}^{n\times m} \qquad \text{and} \qquad \mathbf{Z} := \begin{bmatrix} z_1(t) \\ \vdots \\ z_m(t) \end{bmatrix} \in \mathbb{R}^m \ .$$

Introducing the approximation in Eq. (24) into Eq. (22) and premultiplying by $\boldsymbol{\Xi}^T$ yields the modified system of equations

$$\boldsymbol{\Xi}^T\mathbf{M}_{\mathbf{uu}}\boldsymbol{\Xi}\ddot{\mathbf{Z}} + \boldsymbol{\Xi}^T\mathbf{K}_S\boldsymbol{\Xi}\mathbf{Z} = \boldsymbol{\Xi}^T\mathbf{F} \ , \tag{25}$$

which we note is of size m rather than the original size n. In practical applications it is possible to choose $m \ll n$. This enables the possibility to build a Reduced Order Model (ROM) that approximates the finite element solution in a very efficient manner since the size of the problem to be solved is greatly reduced. In the structural mechanics context, such ROM is commonly referred to as modal analysis.

An important reason for the success of the modal analysis is that the arrays of nodal values of displacement modes are orthogonal both with respect to matrix $\mathbf{M}_{\mathbf{uu}}$ and with respect to matrix $\mathbf{K}_S$. This makes the ordinary system of differential equations in Eq. (25) to be diagonal, i.e., consisting of m decoupled equations.

Remark 4. In this case, we defined the modal analysis based on the statically condensed problem as the ε^v field likely has no practical utility in the sense that its effect onto $\mathbf{u}$ is already taken into account. Nevertheless, if required, the same idea can be applied to the ε^v field by introducing

$$\boldsymbol{\mathcal{E}}^v(t) = \sum_{i=1}^{n} z_i(t)\boldsymbol{\Psi}_i \ .$$

By doing so and applying the previously described procedure one can obtain a ROM that also includes ε^v as an unknown.

Remark 5. A stability and convergence analysis similar to that performed in [16] can be also carried out for the present formulation. In essence, now one has to account for a mass-matrix-like term in the equation for the volumetric strain, although this poses no difficulty, as this matrix is symmetric and positive definite. The conclusion of this analysis, that will be verified in the numerical examples, is that the error in the displacement modes decreases as the inverse of the first discarded eigenvalue ω^2_{m+1}.

6. Numerical results

In this section we present several 2D and 3D numerical experiments to assess the correctness and performance of our proposal, both in the compressible and incompressible regimes. The results described in this section have been obtained with the Kratos Multiphysics open-source finite element framework (Kratos) [20, 21]. For the GEVP resolution, we leverage both Eigen and SciPy libraries [22]. Both pre–processing and and mesh generation have been done by means of the GiD simulation software (GiD). All units are assumed to correspond to the SI.

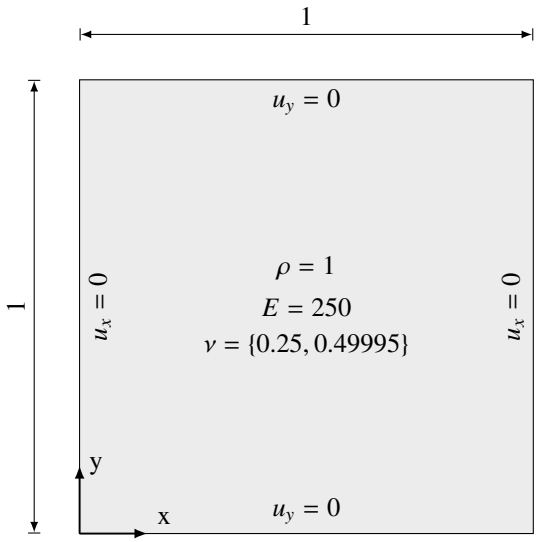

Figure 1: Unit square problem. Geometry, material and boundary conditions.

6.1. Unit square problem

In this first example we study the eigenvalue convergence by solving the GEVP on a unit square domain. As depicted in Fig. 1, we consider a material with Young modulus $E = 250$ and Poisson coefficient $\nu = 0.25$ (compressible case) and $\nu = 0.49995$ (incompressible case) and unit density. The displacement boundary conditions (BCs) are also described in Fig. 1. As it can be observed, a roller support is considered in all the boundaries, meaning that $u_y = 0$ in the horizontal boundaries and $u_x = 0$ in the vertical ones. In this regard, we would like to mention that preliminary experiments with completely clamped BCs reported a slight convergence deterioration associated to the singularities appearing in the corners, which lead to a lack of regularity in the problem. We solve the problem for a set of structured linear quadrilateral and triangular meshes of 2^n edge divisions, being $n = 2, 3, 4, 5, 6$. In the compressible case, we compare the obtained results with those obtained with an irreducible case while in the incompressible one we do so by using a Bbar (Q_1/P_0) formulation. The reference values ($\bar{\lambda}_i$) are obtained by solving the same problem with an overkill mesh made of 1.5M linear quadrilateral (irreducible or Bbar) elements.

Prior to any discussion, we note that we also use this problem to calibrate the algorithmic constants appearing in the stabilisation parameters $\tau_{\mathbf{u}}$ and τ_{ε^v}. Hence, from now on we set the algorithmic constants to $c_1 = 1$ and $c_2 = 4$, respectively.

Figs. 2 and 3 present the convergence of the first six eigenvalues for the compressible case using quadrilateral and triangular meshes, respectively. Similarly, Figs. 4 and 5 present the same results for the incompressible case. As it can be observed, in all cases the OSGS approach convergences with the optimal rate, which is $O(h^2)$. For the compressible case, the OSGS error is slightly larger than that of the irreducible reference values, something that can be perfectly expected as a side effect of the stabilisation. Regarding the incompressible case, the performance of the OSGS quadrilateral is pretty similar to that of the Bbar element. Complementary, we also study the behaviour of an inconsistent ASGS approach. By inconsistent ASGS we mean solving the GEVP using the mass and stiffness matrices resulting from the variational mechanical problem (Eq. (16)), something that one might eventually be tempted to do. The first and most evident thing is that the problem is no longer symmetric, thus requiring the use of a much more inefficient solver for generic dense matrices. Furthermore, we also note that negative eigenvalues appear in some cases. Specifically, the ASGS values in Figs. 2, 3 and 4 are not the first six eigenvalues but the first six positive ones. Surprisingly, the inconsistent ASGS (positive) eigenvalues converge not only with the expected quadratic order but also with a similar error constant to that of the OSGS approach. Nevertheless, we highlight that the spectral theorem no longer holds in the inconsistent ASGS case, something that results into a limitation for the modal analysis application as the mass matrix does not diagonalise anymore. Altogether, these observations evince the practical advantages of the OSGS, which will be our method of choice for the remaining examples of the paper.

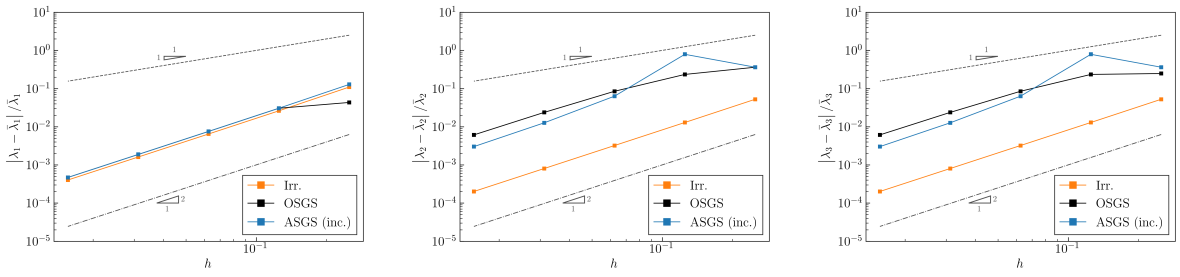

(a) 1st eigenvalue. (b) 2nd eigenvalue. (c) 3rd eigenvalue.

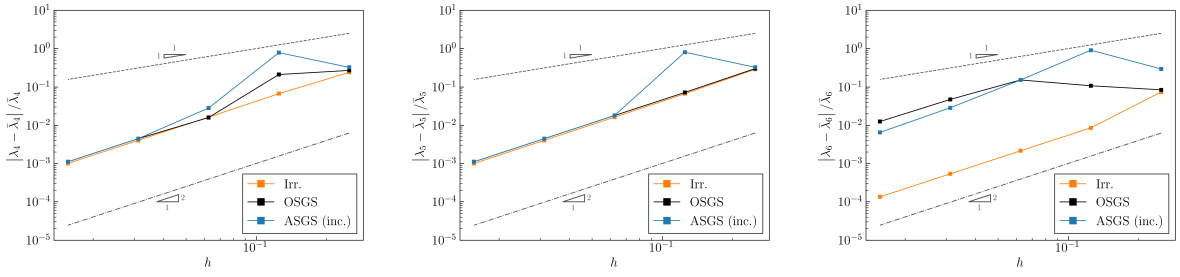

(d) 4th eigenvalue. (e) 5th eigenvalue. (f) 6th eigenvalue.

Figure 2: Unit square problem. Eigenvalue convergence for irreducible, OSGS and inconsistent ASGS quadrilateral elements ($\nu = 0.25$).

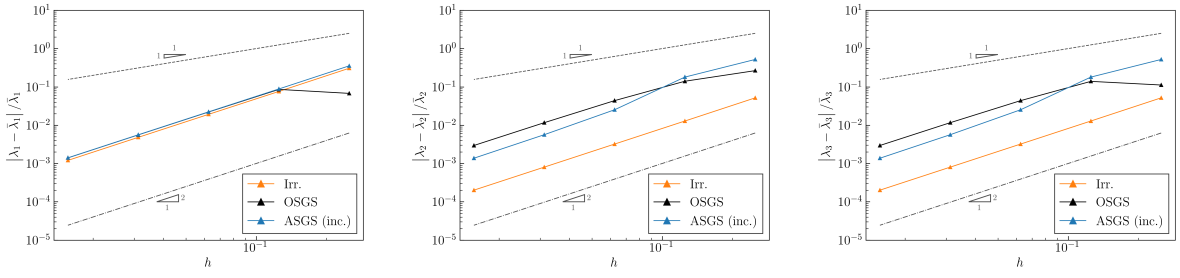

(a) 1st eigenvalue. (b) 2nd eigenvalue. (c) 3rd eigenvalue.

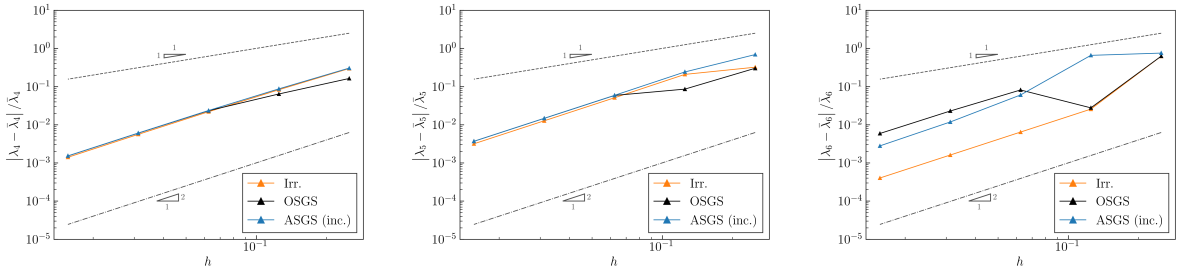

(d) 4th eigenvalue. (e) 5th eigenvalue. (f) 6th eigenvalue.

Figure 3: Unit square problem. Eigenvalue convergence for irreducible, OSGS and inconsistent ASGS triangular elements ($\nu = 0.25$).

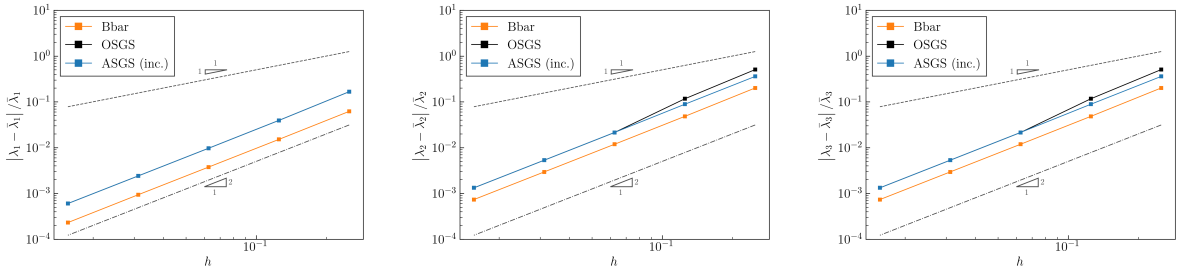

(a) 1st eigenvalue. (b) 2nd eigenvalue. (c) 3rd eigenvalue.

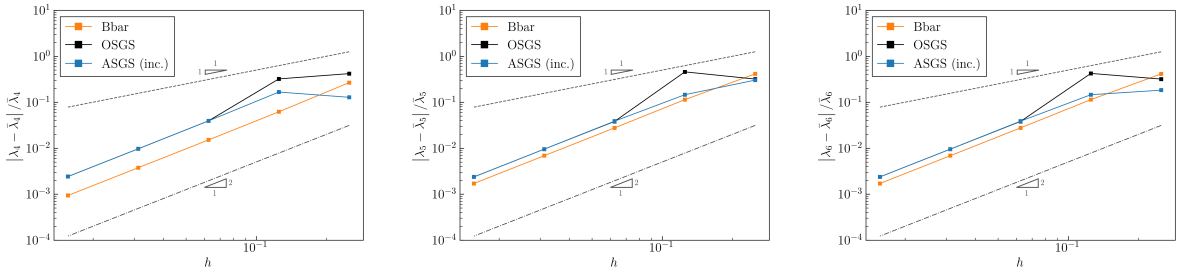

(d) 4th eigenvalue. (e) 5th eigenvalue. (f) 6th eigenvalue.

Figure 4: Unit square problem. Eigenvalue convergence for Bbar, OSGS and inconsistent ASGS quadrilateral elements ($\nu = 0.49995$).

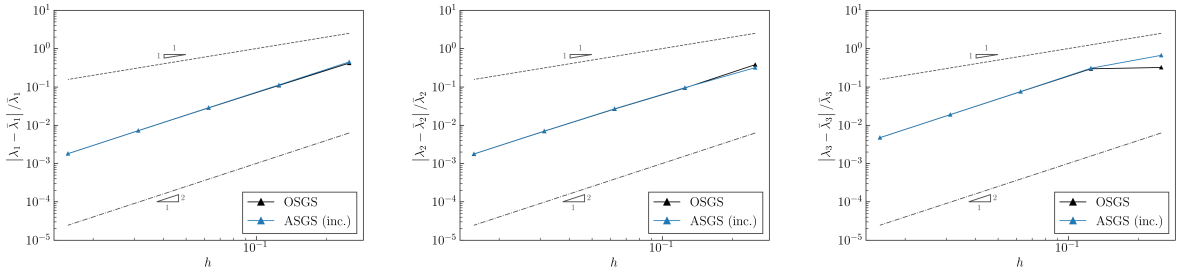

(a) 1st eigenvalue. (b) 2nd eigenvalue. (c) 3rd eigenvalue.

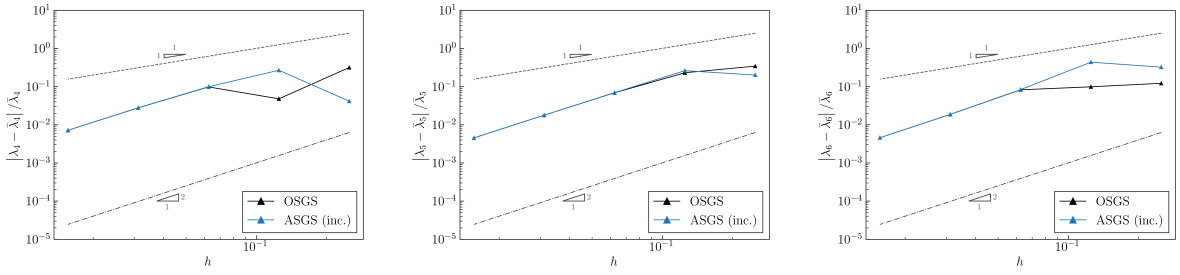

(d) 4th eigenvalue. (e) 5th eigenvalue. (f) 6th eigenvalue.

Figure 5: Unit square problem. Eigenvalue convergence for OSGS and inconsistent ASGS triangular elements ($\nu = 0.49995$).

6.2. Free vibration of a cantilever beam

In this example, which has been previously presented in [16], we analyse the vibration of a 10×1 cantilever beam. The material properties are $\rho = 1$, $E = 3 \cdot 10^3$ and $\nu = 0.49995$. The beam is clamped at its left edge while the other three edges are free. The vibration is induced by the displacement initial condition, which is obtained as the solution of a static problem with an enforced displacement of $1 \cdot 10^{-2}$ along the right edge (see Fig. 2 in [16]). The initial velocity and acceleration are assumed to be zero. For the time discretisation we use a second order backward differentiation formula, to which from now on we refer to as the finite difference (FD) approximation. Hence, the acceleration for a time step i is computed with the previous steps solutions and the time step increment δt as

$$\ddot{\mathbf{U}}(t_i) \approx \frac{-\mathbf{U}(t_{i-3}) + 4\mathbf{U}(t_{i-2}) - 5\mathbf{U}(t_{i-1}) + 2\mathbf{U}(t_i)}{\delta t^2} \, .$$

The problem is solved for a total time $t = 20$, which comprises two complete periods of oscillation. Regarding the time increment, we set $\delta t = 1.0 \cdot 10^{-3}$ so as to ensure properly capturing the high frequency contributions. The domain is discretized with a 100×10 divisions structured mesh of linear triangular elements. As it is discussed in [16], this mesh provides sufficient resolution to consider the first ten eigenfrequencies to be converged.

First, we present the first eight displacement eigenmodes in Fig. 6. As it can be observed, these are mainly bending modes, except modes 4 (Fig. 6d) and 7 (Fig. 6g) which are pure compression (or tensile) modes.

Besides, we also discuss the error of the ROM which, as it is detailed in [16], can be computed with the norm

$$\|\mathbf{U} - \mathbf{U}_m\|_M^2 = \sum_{i,j=m+1}^{n} z_i z_j \boldsymbol{\phi}_i^T \mathbf{M} \boldsymbol{\phi}_j \, .$$

In the previous expression n denotes the number of modes of the reference solution while m is the number of modes used in the ROM. Therefore, $\|\mathbf{U} - \mathbf{U}_m\|_M$ effectively turns into a measure of the error associated to the lack of modes from $m+1$ up to n. Additionally, we also introduce the norm

$$\|\mathbf{U}\|_K^2 = \sum_{i,j=1}^{n} z_i z_j \boldsymbol{\phi}_i^T \mathbf{K} \boldsymbol{\phi}_j \, ,$$

that we will use to normalize the $\|\mathbf{U} - \mathbf{U}_m\|_M$ values. Hence, Fig. 7 depicts the behaviour of $\|\mathbf{U} - \mathbf{U}_m\|_M / \|\mathbf{U}\|_K$, which is computed with a reference solution of $n = 100$ modes, with respect to the value of the corresponding eigenvalue λ_{m+1}. These results are computed at $t = 5$, that is the instant at which the maximum deflection occurs (Fig. 8). Hence, increasing the number of modes successively improves the reconstructed solution, except for the pure compression modes, which have no impact in the error. This is not surprising considering the problem at hand, which main contribution comes from the bending.

The previous observations are also evinced by Fig. 8, which compares the vertical displacement at the upper right node of the beam obtained with the standard dynamic solver (FD) to that of the ROMs featuring 2, 8 and 100 modes. As expected, the differences between the reference FD solution and the 100 modes ROM one are imperceptible. Furthermore, we highlight the remarkably good performance of the 8 mode ROM, which is capable to reproduce the high frequency vibrations (Fig. 8b). Indeed, we dare say that the 2 modes ROM offers a reasonably good approximation taking into account the simplicity of the reconstructed model. In this regard, we would like to point out that a very small time step is required to capture the tiny transient oscillations, which are skipped otherwise. In other words, setting a larger time step makes all the ROM solutions to match the reference one as the error becomes governed by the time integration rather than by the number of modes.

Additionally, we use this example to evaluate the over dissipation effect introduced by the stabilisation when solving problems far from the nearly incompressible limit. Hence, we consider the same time evolution problem but with $\nu = 0.3$ in order to compare both ASGS and OSGS stabilization approaches with a reference irreducible formulation. We make clear that this comparison is based on the standard problem results as the creation of ASGS-based ROMs is limited by the aforementioned complexities of the ASGS GEVP. For the sake of simplicity, we use our in-house transient solver with a 2nd order Backward Differentiation Formula (BDF2) and $\delta t = 1.0 \cdot 10^{-2}$. Again, we use the vertical displacement at the upper right node of the beam as reference magnitude. As it can be observed in

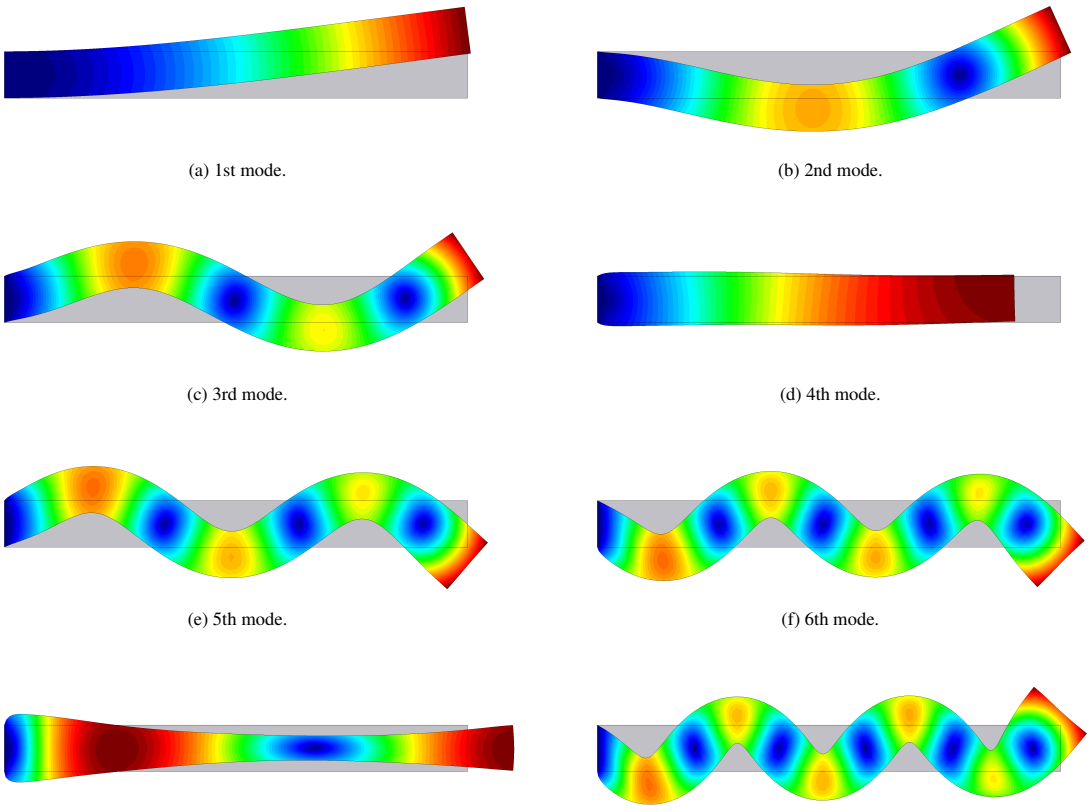

(a) 1st mode. (b) 2nd mode.

(c) 3rd mode. (d) 4th mode.

(e) 5th mode. (f) 6th mode.

(g) 7th mode. (h) 8th mode.

Figure 6: Free vibration of a cantilever beam ($\nu = 0.49995$). First eight displacement modes.

Fig. 9, the ASGS and OSGS displacement evolution show a slight delay with respect to the reference irreducible one. We also note that the over dissipation associated to the stabilisation is more evident in the ASGS case, which phase error becomes apparent during the first oscillation cycle. On the contrary, the OSGS solution is in almost perfect agreement with the irreducible one during the entire first oscillation cycle, being the differences appreciable only during the second one.

6.3. Cook's membrane

In this example we solve the well-known Cook's membrane problem in a transient regime. As depicted in Fig. 10, the material properties are $E = 250$, $\nu = 0.49995$ and $\rho = 1$. The membrane is clamped along its left edge (i.e., $\mathbf{u} = \mathbf{0}$) and a vertical shear load of $6.25 \cdot 10^{-3}$ is applied to the right one. The problem is solved for a total time of 5.5 using the previously described FD scheme with a time step $\delta t = 0.05$ and zero initial conditions for the displacement, velocity and acceleration. Concerning the space discretisation, we use a 36×36 division structured mesh made up with linear triangular elements. As it is discussed in [16], this resolution is sufficient to consider the first eigenvalue to be converged.

We start the discussion by showing the first eight eigenmodes in Fig. 11. As it can be observed, these represent different bending configurations, all of them relevant to the problem at hand. This is evinced in Fig. 12, which presents the ROM solution error with respect to the eigenvalues at time $t = 1.5$. As in the previous example, the reference solution is computed considering $n = 100$ modes. Hence, we note that in this case, in which the shear component is the main contribution inducing the bending, the initial error decay es more progressive than in the

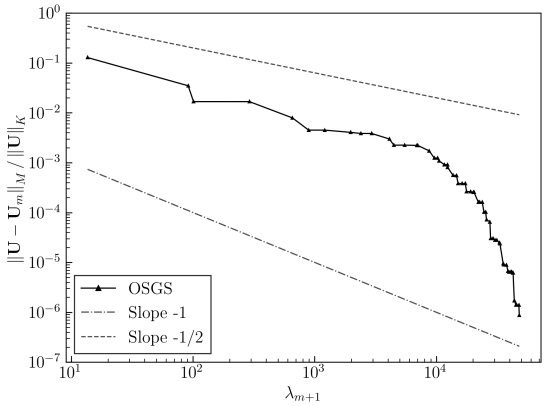

Figure 7: Free vibration of a cantilever beam ($\nu = 0.49995$). Variation of the error with respect to the eigenvalues at $t = 5$.

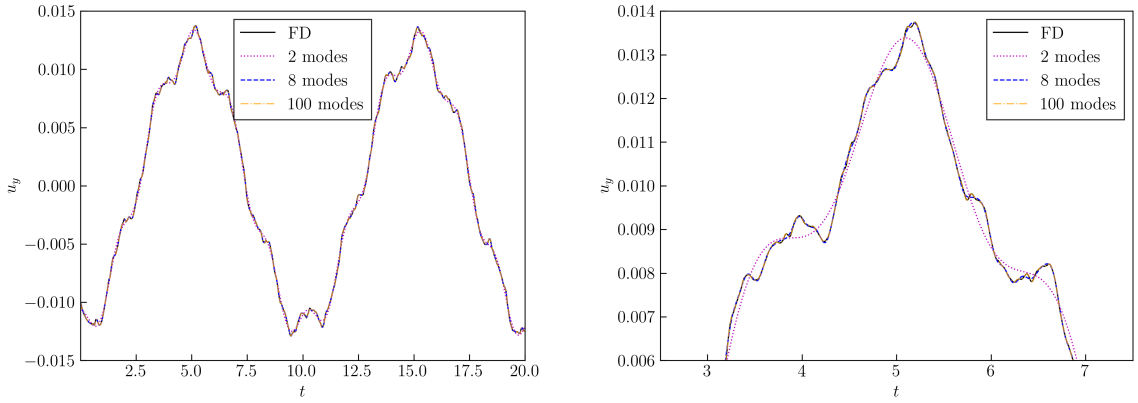

(a) Complete analysis.

(b) Zoom at the time interval $[2.5, 7.5]$.

Figure 8: Free vibration of a cantilever beam ($\nu = 0.49995$). Transient behaviour of the vertical displacement at the tracking point.

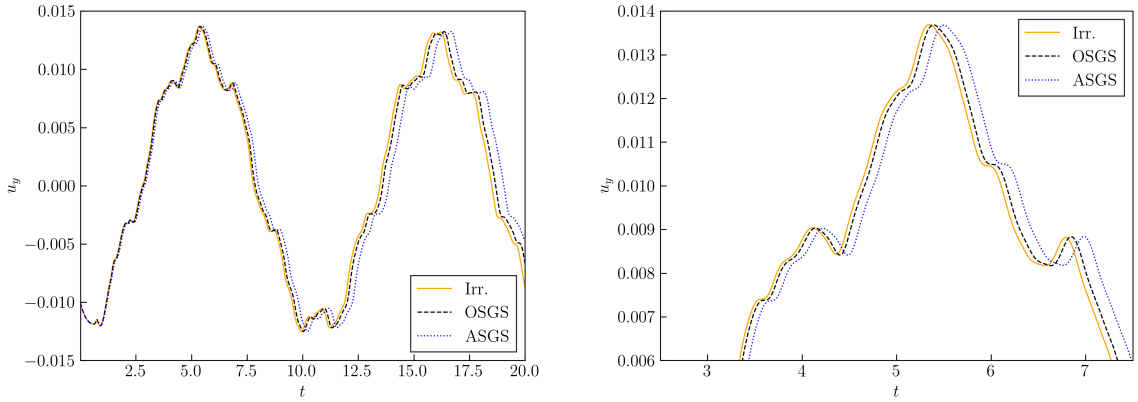

(a) Complete analysis.

(b) Zoom at the time interval $[2.5, 7.5]$.

Figure 9: Free vibration of a cantilever beam ($\nu = 0.3$). Transient behaviour of the vertical displacement at the tracking point.

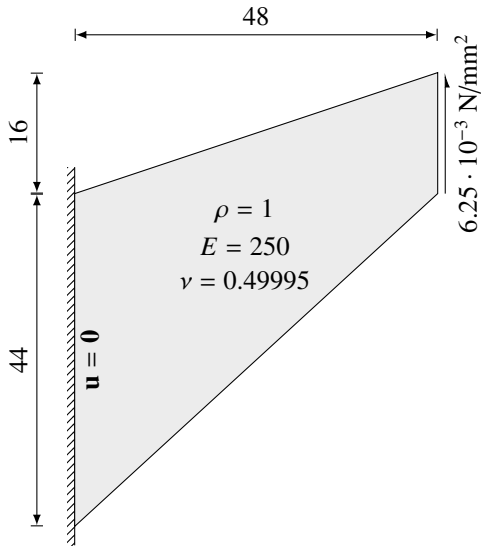

Figure 10: Cook's membrane. Geometry, material and boundary conditions.

previous example, meaning that the very first modes (i.e., those associated to the lowest frequencies) play an important role in reconstructing the solution.

Complementary, in Fig.13a we compare the vertical displacement at the upper right corner of the membrane obtained with the standard dynamic solver (FD) to that of the ROMs featuring 8 and 100 modes. The ROM results are in remarkably good agreement with the reference FD solution. In particular, the 100 mode solution almost perfectly matches the expected values. Regarding the 8 mode solution, we report a tiny underestimation of the oscillation amplitude. Notwithstanding, we think that the ability of the method in returning a very good approximation to the solution with such very few modes deserves to be highlighted.

6.4. Twisting column

In this last example we simulate a column subjected to a pure torsion load. Besides allowing us to test our three-dimensional implementation, this test is specifically conceived to assess the behaviour of the model in presence of torsion, something not doable with the aforementioned bending-dominated examples. The problem geometry consists in a $1 \times 1 \times 6$ column made with the previous example material, that is $E = 250$, $\nu = 0.49995$ and $\rho = 1$. Again, we use the previously mentioned FD scheme for the time integration, in this case with a total time $t = 5$ and $\delta t = 0.01$. The geometry is discretised with a $5 \times 5 \times 30$ divisions structured mesh made with linear hexahedral elements. The motion is induced by setting as initial displacement field the values resulting from solving a steady problem with the in-plane rotation displacement field

$$
\begin{aligned}
u_x &= x(\cos(0.00175) - 1.0) - y\sin(0.0175)\ , \\
u_y &= x\sin(0.0175) + y(\cos(0.0175) - 1.0)\ , \\
u_z &= 0.0
\end{aligned}
$$

enforced at the top surface. The initial velocity and acceleration are considered to be zero.

As in the previous examples, we start by discussing the modes associated to the first eight frequencies in Fig. 14. It can be clearly noted that this set of modes includes simple bending (modes 1 and 2), multiple bending (modes 4, 5, 7 and 8), pure torsion (mode 3) and pure compression (mode 6) deformation modes. This is also evinced in Fig. 15, which presents the error or the ROM according to the number of modes for $t = 2.8$ (i.e., the instant at which the maximum rotation takes place). Again, a reference solution of $n = 100$ modes is used for the error calculation. Hence, it becomes apparent that the error remains constant until the addition of the third mode, which corresponds to torsion deformation. The same behaviour is observed for the subsequent bending and pure compression modes, which add no value to the approximation.

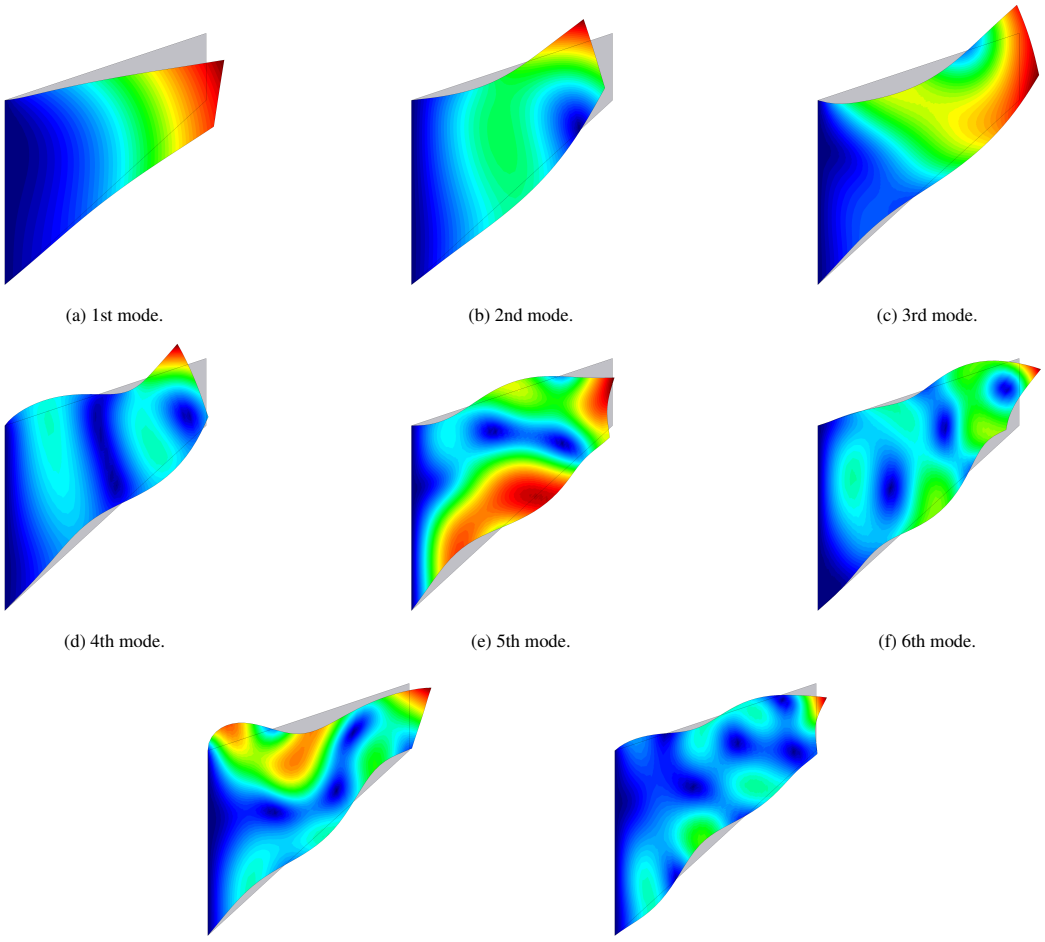

(a) 1st mode. (b) 2nd mode. (c) 3rd mode.

(d) 4th mode. (e) 5th mode. (f) 6th mode.

(g) 7th mode. (h) 8th mode.

Figure 11: Cook's membrane. First eight displacement modes.

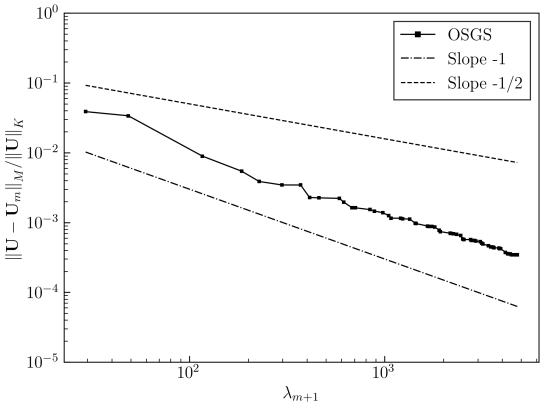

Figure 12: Cook's membrane. Variation of the error with respect to the eigenvalues at $t = 1.5$.

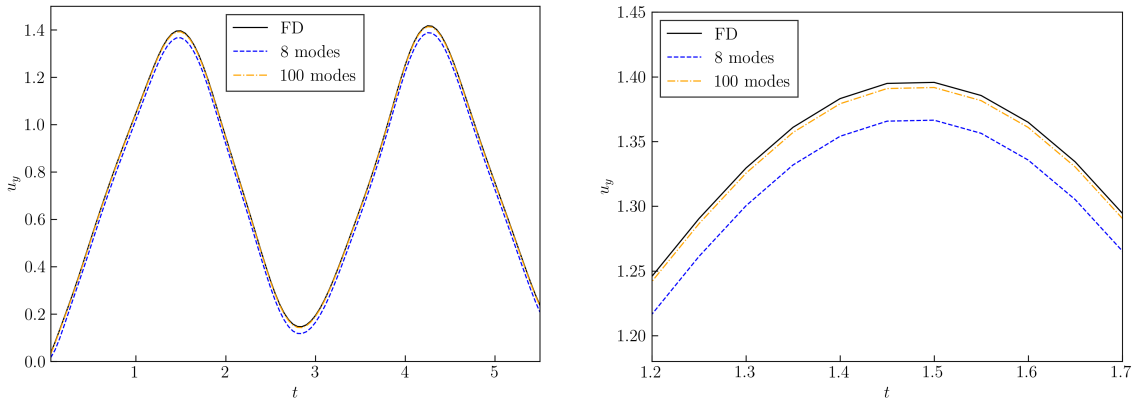

(a) Complete analysis.

(b) Zoom at the time interval [1.2, 1.7].

Figure 13: Cook's membrane. Transient behaviour of the vertical displacement at the tracking point.

Furthermore, we also study the evolution of the in-plane displacements (u_x and u_y) for a control point located at one of the corners of the top surface. In this case, we compare the FD reference solution to that of the ROM considering 8 and 100 modes. As it can be expected, the 100 mode solution has an extremely good correlation with the reference one. However, we see that, as a difference to previous examples, the 8 modes approximation is not sufficient to properly capture the problem behaviour, something that is associated to the insufficient number of torsional modes in the approximation.

7. Conclusion

In this paper we have extended the **u**-ε^{ν} formulation previously presented in [7] to dynamic problems, thus enabling the resolution of (nearly) incompressible mechanical problems. This formulation is specially conceived to be used in presence of equal-order finite element approximations, thus enabling the efficient simulation of complex geometries possibly requiring unstructured meshes. The downside is the need of stabilisation as the interpolation pair used is not inf-sup stable. In this regard, we have explored the application of two VMS-based approaches, namely the ASGS and the OSGS methods. Though both techniques are perfectly valid for the transient problem, the limitations of the ASGS become evident when focusing on the corresponding GEVP. Specifically, the use of the ASGS approach leads to a quadratic GEVP despite the linearity of the original problem. Aiming at circumventing such inconvenience, we also study the behaviour of solving the GEVP with the ASGS mass and stiffness matrices resulting from the standard dynamic problem, leading to an inconsistent ASGS eigenvalue problem formulation. On top of resulting in a non-symmetric GEVP, which requires the use of inefficient eigenvalue algorithms for generic dense matrices, the inconsistent ASGS problem yields negative eigenvalues. However, using the OSGS technique results in an optimally convergent linear GEVP which algebraic form involves symmetric matrices only, thus enabling the use of highly optimised eigenvalue solvers for sparse Hermitian matrices. Additionally, we also describe how such GEVP algebraic form can be exploited to create highly efficient ROMs based on the classical modal analysis. The advantages and convergence of the method as well as the performance of the resulting ROMs are proved by solving a series of two- and three-dimensional problems involving (nearly) incompressible materials.

CRediT authorship contribution statement

Rubén Zorrilla: Conceptualization, Software, Validation, Investigation, Writing - Original Draft, Writing - Review & Editing, Visualization. **Riccardo Rossi:** Conceptualization, Writing - Review & Editing, Funding acquisition. **Ramon Codina:** Formal analysis, Writing - Review & Editing, Supervision.

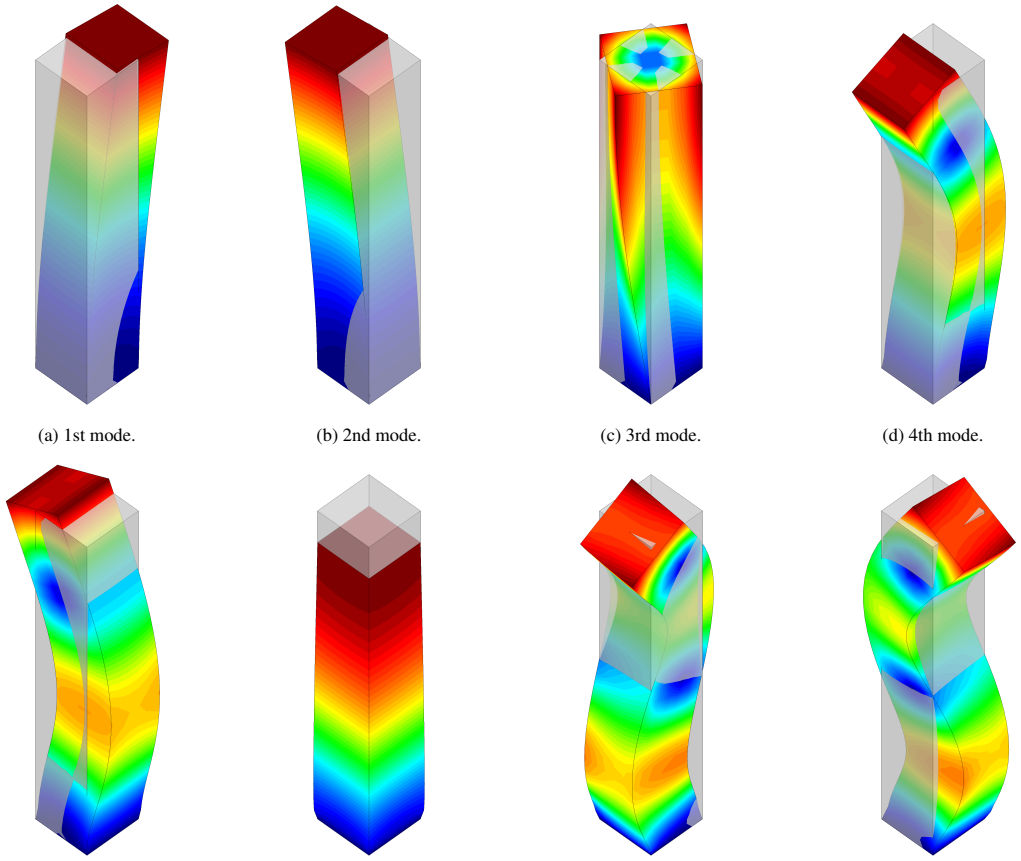

(a) 1st mode. (b) 2nd mode. (c) 3rd mode. (d) 4th mode.

(e) 5th mode. (f) 6th mode. (g) 7th mode. (h) 8th mode.

Figure 14: Twisting column. First eight displacement modes.

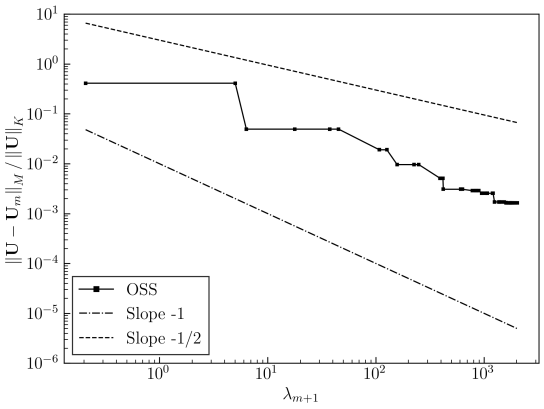

Figure 15: Twisting column. Variation of the error with respect to the eigenvalues at $t = 2.8$.

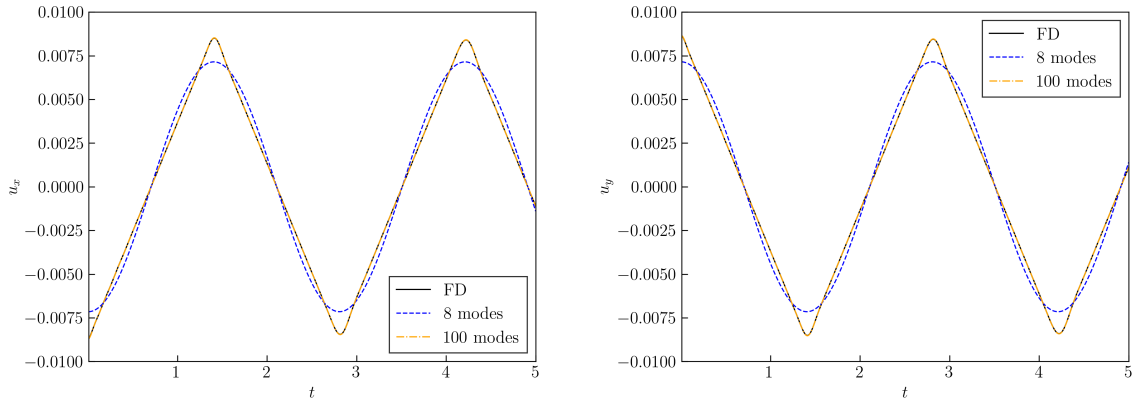

(a) u_x. (b) u_y.

Figure 16: Twisting column. Transient behaviour of the in-plane displacements at the tracking point.

Declaration of competing interest

The authors declare that they have no known competing financial interests or personal relationships that could have appeared to influence the work reported in this paper.

Data availability

Data will be made available on request.

Acknowledgments

The authors gratefully acknowledge Mr. Hauke Gravenkamp for the unit square problem regularity and boundary conditions discussions. Rubén Zorrilla and Riccardo Rossi acknowledge the research project TED2021-130471B-I00, financed by MICIU/ AEI /10.13039/501100011033 and by the "European Union Next GenerationEU/ PRTR". Ramon Codina acknowledges the support received from the ICREA Acadèmia Research Program of the Catalan Government.

References

[1] E. A. de Souza Neto, F. M. Andrade Pires, D. R. J. Owen, F-bar-based linear triangles and tetrahedra for finite strain analysis of nearly incompressible solids. Part I: formulation and benchmarking, International Journal for Numerical Methods in Engineering 62 (3) (2005) 353–383.

[2] J. Kim, K.-J. Bathe, The finite element method enriched by interpolation covers, Computers & Structures 116 (2013) 35–49.

[3] E. A. de Souza Neto, D. Perić, M. Dutko, D. R. Owen, Design of simple low order finite elements for large strain analysis of nearly incompressible solids, International Journal of Solids and Structures 33 (20) (1996) 3277–3296.

[4] T. J. R. Hughes, Generalization of selective integration procedures to anisotropic and nonlinear media, International Journal for Numerical Methods in Engineering 15 (9) (1980) 1413–1418.

[5] T. J. Hughes, G. R. Feijóo, L. Mazzei, J.-B. Quincy, The variational multiscale method—a paradigm for computational mechanics, Computer Methods in Applied Mechanics and Engineering 166 (1) (1998) 3 – 24, advances in Stabilized Methods in Computational Mechanics.

[6] M. Chiumenti, Q. Valverde, C. Agelet de Saracibar, M. Cervera, A stabilized formulation for incompressible elasticity using linear displacement and pressure interpolations, Computer Methods in Applied Mechanics and Engineering 191 (46) (2002) 5253–5264.

[7] R. Rossi, R. Zorrilla, R. Codina, A stabilised displacement–volumetric strain formulation for nearly incompressible and anisotropic materials, Computer Methods in Applied Mechanics and Engineering 377 (2021) 113701.

[8] M. Cervera, M. Chiumenti, R. Codina, Mixed stabilized finite element methods in nonlinear solid mechanics: Part I: Formulation, Computer Methods in Applied Mechanics and Engineering 199 (37) (2010) 2559 – 2570.

[9] R. Codina, Finite element approximation of the three field formulation of the Stokes problem using arbitrary interpolations, SIAM Journal on Numerical Analysis 47 (2009) 699–718.

[10] M. Chiumenti, M. Cervera, R. Codina, A mixed three-field FE formulation for stress accurate analysis including the incompressible limit, Computer Methods in Applied Mechanics and Engineering 283 (2015) 1095–1116.
[11] G. Scovazzi, R. Zorrilla, R. Rossi, A kinematically stabilized linear tetrahedral finite element for compressible and nearly incompressible finite elasticity, Computer Methods in Applied Mechanics and Engineering 412 (2023) 116076.
[12] G. Scovazzi, B. Carnes, X. Zeng, S. Rossi, A simple, stable, and accurate linear tetrahedral finite element for transient, nearly, and fully incompressible solid dynamics: a dynamic variational multiscale approach, International Journal for Numerical Methods in Engineering 106 (10) (2016) 799–839.
[13] N. M. Lafontaine, R. Rossi, M. Cervera, M. Chiumenti, Explicit mixed strain-displacement finite element for dynamic geometrically non-linear solid mechanics, Computational Mechanics 55 (3) (2015) 543–559.
[14] M. Cervera, N. M. Lafontaine, R. Rossi, M. Chiumenti, Explicit mixed strain–displacement finite elements for compressible and quasi-incompressible elasticity and plasticity, Computational Mechanics 58 (3) (2016) 511–532.
[15] Ö. Türk, D. Boffi, R. Codina, A stabilized finite element method for the two-field and three-field Stokes eigenvalue problems, Computer Methods in Applied Mechanics and Engineering 310 (2016) 886–905.
[16] R. Codina, O. Türk, Modal analysis of elastic vibrations of incompressible materials using a pressure-stabilized finite element method, Finite Elements in Analysis and Design 206 (2022) 103760.
[17] R. Codina, S. Badia, J. Baiges, J. Principe, Variational Multiscale Methods in Computational Fluid Dynamics, John Wiley & Sons, Ltd., 2017, pp. 1–28.
[18] R. Codina, Stabilization of incompressibility and convection through orthogonal sub-scales in finite element methods, Computer Methods in Applied Mechanics and Engineering 190 (13) (2000) 1579–1599.
[19] R. Codina, Analysis of a stabilized finite element approximation of the Oseen equations using orthogonal subscales, Applied Numerical Mathematics 58 (3) (2008) 264–283.
[20] P. Dadvand, R. Rossi, E. Oñate, An object-oriented environment for developing finite element codes for multi-disciplinary applications, Archives of Computational Methods in Engineering 17 (3) (2010) 253–297.
[21] P. Dadvand, R. Rossi, M. Gil, X. Martorell, J. Cotela, E. Juanpere, S. R. Idelsohn, E. Oñate, Migration of a generic multi-physics framework to HPC environments, Computers & Fluids 80 (2013) 301 – 309.
[22] P. Virtanen, R. Gommers, T. E. Oliphant, M. Haberland, T. Reddy, D. Cournapeau, E. Burovski, P. Peterson, W. Weckesser, J. Bright, S. J. van der Walt, M. Brett, J. Wilson, K. J. Millman, N. Mayorov, A. R. J. Nelson, E. Jones, R. Kern, E. Larson, C. J. Carey, İ. Polat, Y. Feng, E. W. Moore, J. VanderPlas, D. Laxalde, J. Perktold, R. Cimrman, I. Henriksen, E. A. Quintero, C. R. Harris, A. M. Archibald, A. H. Ribeiro, F. Pedregosa, P. van Mulbregt, SciPy 1.0 Contributors, SciPy 1.0: Fundamental Algorithms for Scientific Computing in Python, Nature Methods 17 (2020) 261–272.